Airlift Bioreactors: Analysis of Local Two-Phase Hydrodynamics

Mark A. Young, Ruben G. Carbonell, and David F. Ollis
Dept. of Chemical Engineering, North Carolina State University, Raleigh, NC 27695

Local two-phase flow measurements were obtained in a pilot-scale, external-loop airlift bioreactor using hot-film anemometry and resistivity probe techniques. The radial dependence of both gas and liquid velocities and of the void fraction was substantial. Developing flow effects were pronounced, as evidenced by distinct changes in the radial profiles of fluid flow properties with axial position. For high gas flow rates, liquid acceleration effects near the sparger resulted in greatly reduced slip velocities in a substantial portion of the riser. A significant reduction in mass transfer may occur under such conditions.

The point equations of continuity and motion were used to develop a differential, two-fluid model for two-phase flow in airlift risers. The only empirical parameters in the model represent frictional effects. The developing two-phase flow characteristic of airlift risers was observed to create significantly higher frictional effects at the wall than is routinely observed for fully-developed flow. Model predictions were compared to our own experimental results as well as those of Merchuk and Stein (1981). Agreement between the predicted and measured values was typically within 10% for both cases.

Introduction

Due to their simple construction and economical mixing characteristics, airlift bioreactors were employed first in industrial applications requiring high mass transfer and good mixing, most notably for large-scale, aerobic production of microbial (single cell) protein. However, airlift reactor performance is sufficiently versatile to prompt its use in a range of applications. Bench-scale airlift fermentors are now commercially available. Owing to the diffuse nature of the power dissipation through the expansion of the sparging gas, these units may be used to good advantage for shear-sensitive cultures. Alternatively, researchers have utilized the airlift design for applications involving non-Newtonian broths, such as fermentation of filamentous fungi (Barker and Wogan, 1981; Malfait et al., 1981) and plant cell culture (Townsley et al., 1983). Onken and Weiland (1983) have cited other possible bioreactor applications, including the production of citric acid and xanthan gum.

A wide range of experimental studies of airlift hydrodynamics have been conducted in recent years. However, quantitative comparison of published results is frequently hampered by the lack of experimental consistency between studies and by incomplete reporting of experimental conditions. Many of the correlations presented in the literature are restricted in their validity to the same reactor size, type and gas-liquid system used in their development. In this vein, several researchers have stressed the need for study of larger-scale reactors (e.g., Bello et al., 1985; Blenke, 1979; Kleinstreuer and Poweigha, 1984).

The hydrodynamic quantities that have been examined to date include phase velocities, flow regimes, and gas-phase volume fraction. Each of these quantities may be influenced by the various design and operating features. Liquid velocity has been analyzed almost exclusively by the use of tracers (Weiland, 1984; Jones, 1985; Koide et al., 1984; Fields and Slater, 1983). Limited local measurements of annular liquid velocity were made by Koide et al. (1988) using a heat flux technique. Only integrated, averaged data were reported. In general, liquid mixing times have been shown to decrease steeply for initial increases in gas sparging rate and to approach an asymptotic

Current address of M. A. Young: Union Carbide Corp., Technical Center, P.O. 8361, South Charleston, WV 25303.

value determined by the ratio of the downward to upward flow areas and the liquid properties. Liquid mixing has been shown to occur primarily in the head and bottom regions of the reactor, rather than via dispersion behind bubbles (Fields and Slater,1983; Weiland, 1984). Mixing times may be minimized by maintaining the unaerated liquid depth in the gas separation zone greater than one or two riser diameters (Fields and Slater, 1983; Sukan and Vardar-Sukan, 1987).

Sparger design affects liquid velocities and mixing, particularly for small-scale reactors. For a given gas flow rate, the sparger configuration influences mixing primarily through changes in mean bubble size and the uniformity of gas-phase distribution. These characteristics in turn affect both gas holdup (and hence liquid velocity) and turbulence intensity. The tremendous variation in sparger design makes quantitative comparison difficult, at best. Other factors such as reactor scale, reactor configuration, and the gas flow range studied also hamper reaching general conclusions. Indeed, two recent studies of concentric tube reactors reported conflicting results concerning sparger effects. Koide et al. (1988) found that the liquid circulation rate increased with increased orifice diameter of the sparger. However, Bovonsombut et al. (1987) found no significant differences in mixing times for multiorifice ring vs. porous plate spargers.

Airlift bioreactors typically operate in the flow regime referred to as bubble flow. Nevertheless, a careful examination of airlift hydrodynamics opens many questions concerning the proper characterization of the flow. A recent study by Popovic and Robinson (1987) underscored this conclusion by recommending examination of the full range of gas-liquid flow from bubble to slug flow. Many investigators have assumed plug flow to prevail in airlift risers. To date, no measurements of local flow phenomena have been presented in the literature either to substantiate or refute this assumption. However, several researchers have suggested possible contradictions to this view. Jones (1985) speculated that local recirculation of liquid within the draft tube resulted in lower than predicted liquid flux in the downcomer of his concentric tube fermentor. Mercer (1981) also suspected deviations from the assumed plug flow behavior in the 15-cm-diameter riser of an external loop reactor. He reported observing downward bubble flow along the riser walls and the formation of circulation cells. Similar questions are raised by the studies of Siegel et al. (1986), Merchuk and Stein (1981), and Orazem et al. (1979). The study by Orazem and coworkers is also noteworthy as being the only published report of local velocity and void measurements, in this case for the downcomer of a split cylinder vessel. Additionally, only a few attempts have been made to quantify the liquid-phase turbulence intensity of airlift bioreactors, most notably by Glasgow et al. (1984) and Jones et al. (1987). The extent to which particular conclusions may be generalized to other reactors and scales frequently was not addressed by the researchers.

Previously, only global or average flow properties have usually been measured. Typically, the average gas volume fraction was ascertained by measurement of the overall volume change of the system upon sparging, for example. Alternatively, axial changes in gas fraction have been estimated via a series of manometer readings taken at locations distributed along the column. Characteristically, the average liquid-phase velocity has been determined using tracers of various descriptions. Gas-phase velocities have not been determined. Pressure changes have sometimes been measured only from the top to the bottom of the column, although a number of studies have included data on the axial dependence of liquid-phase pressure.

Gas-phase volume fraction is a critical characteristic of airlift operation due to its strong influence upon gas-liquid mass transfer. Consequently, numerous studies have been conducted to evaluate the dependence of void fraction upon such basic parameters as the ratio of downward to upward flow area, sparging rate, sparger design, and physicochemical properties (e.g., Koide et al., 1983a,b; Weiland, 1984; Bello et al., 1985; Kawase and Moo Young, 1986a; Merchuk and Stein, 1981). Due to offsetting effects of greater superficial gas velocity and greater liquid velocity in the draft tube, the void fraction varies little with changes in the ratio of downward to upward flow area for concentric tube designs. For external loop configurations, by contrast, increases in downcomer size enhance liquid velocity in the riser without compensating gas velocity increases; void fraction tends to decrease. Sparger design studies indicate that high average void fraction is achieved with multiorifice or porous-plate spargers, as compared to single-orifice designs. This behavior is attributed to the resultant smaller, more evenly distributed bubbles having lower rise velocities and less coalescence (Merchuk and Stein, 1981; Bovonsombut et al., 1987). Gas-phase measurements have been limited most commonly to determination of the overall void fraction by volume change upon sparging. A few studies (e.g., Merchuk and Stein, 1981) reported cross-sectionally averaged void measurements at different axial positions, as determined by manometric techniques.

From a hydrodynamic viewpoint, airlift reactors are unique in that the flow of the gas initiates the liquid flow. The resulting recirculating, two-phase flow has proven to be a challenging modeling problem. The hydrodynamics of airlift reactors have been studied and modeled by numerous researchers, particularly during the last decade. An early study by Freedman and Davidson (1969) analyzed airlift hydrodynamics utilizing a macroscopic momentum balance and ignoring frictional effects. This early effort was a minor aspect of a larger study of bubble column hydrodynamics and was derived for the restrictive case where downcomer liquid velocity equals the terminal bubble rise velocity. More recently, several investigators have developed equations for airlift flow that are based in part on the work of Freedman and Davidson. Koide et al. (1983, 1984) wrote macroscopic momentum balances for the riser and downcomer sections, while describing the flow in the gas separation and sparging regions via macroscopic mechanical energy equations. A range of empirical data were analyzed by this approach, and Koide et al. developed detailed correlations for hydrodynamic effects such as total measured pressure drop in the riser, void fraction in the riser, and downcomer and wall drag effects. Using a similar approach, Hsu and Dudukovic (1980) developed an equation relating internal liquid circulation rates to correlated values of void fraction and wall friction.

Other researchers have employed the continuity-based drift-flux theory of Zuber and Findlay (1965) in combination with the mechanical energy balance to model airlift hydrodynamics. Merchuk and Stein (1981) analyzed data from their external-loop airlift reactor using equations founded upon drift-flux theory and the mechanical energy balance. The drift-flux form

was shown to relate the gas-phase velocity to the mixture volumetric flux using plausible values for the drift-flux parameters. Liquid velocities were accurately correlated with gas sparging rate using a power law form. Verlaan et al. (1986) also incorporated drift-flux and mechanical energy balance concepts into the only model to date which accounts for the axial dependence of hydrodynamic variables. Siegel et al. (1986) also adopted the drift-flux approach in analyzing airlift hydrodynamics.

A third general approach for investigating airlift fluid mechanics has been the application of an energy balance to the expanding, isothermal sparging gas. The total expansion work done by the gas is equated to the sum of various sources of energy dissipation. Recent examples of this approach include Jones (1985), Lee et al. (1987), and Chisti et al. (1988). Models derived from this type of analysis have been successful in predicting the liquid-phase velocity, provided the gas volume fraction is known.

Most models of airlift reactor hydrodynamics have assumed the flow to be homogeneous, i.e., without variation between phases or with spatial position. From the flow profiles reported in this study, it is apparent that the two-phase flow characteristic of airlift reactors is not homogeneous. Significant differences in phase velocities are the norm, and distinct variations in void fraction and phase velocity occur with changes in radial position. Additionally, for large-scale applications, changes in fluid velocities and gas fractions with axial position are expected to be substantial. Consequently, the current model was developed in a two-fluid, differential form to describe changes occurring between phases and axial position.

The principal objective of the present research was to develop both a detailed data set of the local, two-phase fluid mechanics of airlift reactors and a differential, two-fluid model that represents the data. The two-phase hydrodynamics of airlift reactors were examined using a pilot-scale vessel. Four experimental techniques were employed: thermal anemometry, manometry, gamma densitometry, and resistivity probe techniques. Each method is described briefly in the experimental section. Background information regarding each technique and quantitative treatment of its application in this study appears in Young (1989). The experimental data are presented graphically, usually grouped according to the downcomer size used. In addition to local profiles of the primary measured quantities, the local slip velocity between gas and liquid is reported, since it is a commonly used quantity in two-phase flow modeling. The application of drift-flux theory to airlift risers is also addressed. In previous determinations of the drift-flux distribution parameter C_o, the characteristic shapes of the fluid velocity profiles were assumed and C_o evaluated. In contrast, the local transport properties measured in our study permit the direct calculation of drift-flux model parameters for the first time. Calculated parameter values are compared to those deduced or assumed by previous investigators.

The hydrodynamic model was derived from the classic forms of the continuity and momentum equations written for a point in space. This approach assures that all assumptions are explicitly delineated. Each term of the resulting model has a clearly identifiable physical meaning, which is essentially maintained even after empirical representations have been substituted for certain fundamental forms. Prior models have commonly included empirical correlations for both the frictional effects and at least one other aspect of the hydrodynamics, such as the dependence of void fraction or liquid-phase velocity upon gas sparging rate. The present model incorporates empirical expressions for the frictional effects only. Friction appears in three terms in the derived equations: the gas-liquid drag term, the mixture riser section-wall interaction term, and the downcomer liquid-wall term. The model assumes no gas recirculation. Model predictions compare favorably with data taken in external-loop reactors having multiorifice spargers and operated with air and water.

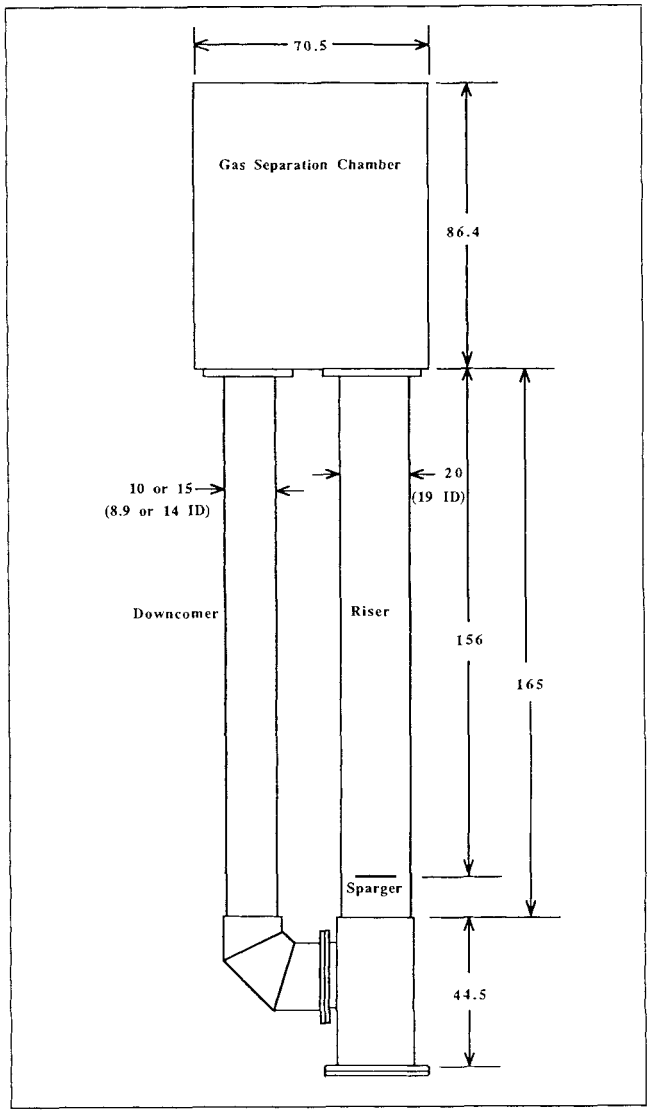

Figure 1. External loop airlift reactor.

The separator chamber is 27.9-cm-wide; dimensions are in centimeters.

Experimental Procedure

Reactor design

An external-loop airlift reactor was designed for this study and fabricated using transparent acrylic plastic, thus allowing visual observation of all flow processes. The reactor design and scale are illustrated in Figure 1; the working liquid volume

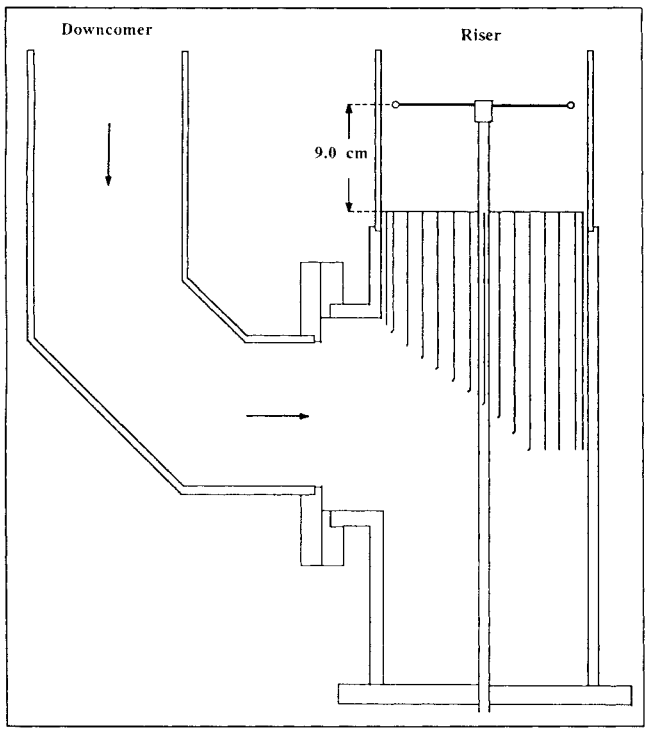

Figure 2. Cross-sectional view of downcomer, straightening vanes and sparger.

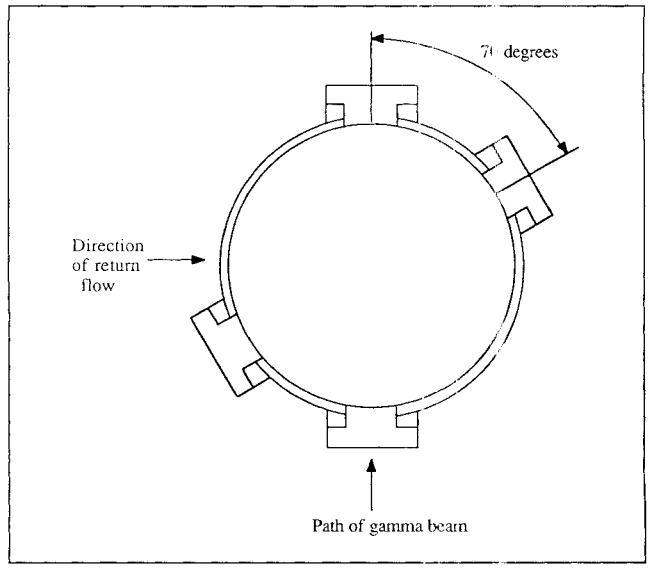

Figure 3. Orientation of sampling ports in riser.

Pairs of sampling ports are located at two axial positions. The lower pair is 71 cm above the sparger, and the upper pair is 132 cm above it. The distance from the sparger to the bottom of the gas separator is 156 cm.

was approximately 160 L when the larger of two interchangeable downcomers (14 and 8.9 cm ID) was used. The downcomer-to-riser diameter ratios were 0.47 and 0.73. The unaerated liquid depth in the separation chamber was held constant at twice the riser ID (i.e., at 38 cm), which was shown by Weiland (1984) to minimize liquid flow resistance in the separation zone. The separation of the gas was nearly complete, with only a negligible fraction of the entering gas being recirculated at the highest sparging rates. Flow straightening vanes were located in the riser at the point of return flow from the downcomer to distribute the liquid phase more evenly prior to sparging. Figure 2 offers a cross-sectional view of the relative placement of the downcomer return, straightening vanes and sparger. The 13 vanes were separated by 2.54-cm gaps and ranged in length from a maximum of 23 cm to a minimum of 12 cm. The bottom 0.6 cm of each vane was bent to a 30-degree angle to further facilitate the flow redirection. Qualitative studies confirmed the presence of more uniform liquid velocity profiles and radial gas distribution in the bottom half of the riser when using these straightening vanes. The additional pressure drop introduced by the presence of the vanes was judged to be small, since visual timing of the liquid recirculation rate using a neutrally buoyant marker indicated no significant difference with or without the straightening vanes in place. The marker was constructed of a 3-cm-long, 0.64-cm-diameter Tygon tubing; the ends were sealed with silicone caulk, and the cavity was filled with sufficient red-tinted water to give the marker the density of water. As noted in subsequent sections, numerous local-phase measurements were made at different axial and radial positions in the riser. For each of two axial positions, the radial profiles of local fluid flow properties were obtained for two azimuthal positions. Figure 3 shows the positioning of the sampling ports on the riser. Although a 90-degree angle between ports would be the most obvious choice, the 70-degree angle was chosen due to spatial constraints imposed by the downcomer position; the arrangement shown still permitted evaluation of the angular uniformity of local property distributions. A single sampling port was located at the midpoint of the downcomer.

Water and air were employed as the gas/liquid system for the duration of the study. The water was initially purified via reverse osmosis, reaching a conductivity of approximately 3 μS. The water was stored in a covered polyethylene barrel between runs and was filtered through a 5-micron particle filter each time the reactor was filled. The gas exit in the top of the separator chamber was covered with a glass wool filter (7-cm-deep) to reduce the introduction of dust particles. The flow of compressed air was filtered, throttled, and regulated prior to measurement using a calibrated rotameter.

Figure 4 schematically represents the ring sparger constructed for this study. The ring configuration allowed the gas to be introduced into the riser without significantly obstructing the flow returning from the downcomer. The hub of the ring and spokes arrangement was a hollow cylinder that was closed at one end and threaded on the other to accommodate the gas supply pipe. The distance from the sparger to the riser exit was 156 cm. The separation between the top of the straightening vanes and the lower sparger surface was 9.0 cm (see Figures 1 and 2). Sparging rates are reported as the superficial gas velocity based on the riser cross-sectional area and corrected to a standard temperature (296.5 K) and the hydrostatic pressure at the sparger (1.206×10^5 Pa). Four different sparging rates were studied, i.e., $J_g = 0.96$, 2.1, 4.6 and 8.2 cm/s. (The highest flow rate for the smaller 8.9-cm downcomer was slightly higher at 8.4 cm/s.) Visual observations indicated that the ellipsoidal bubbles present displayed a narrow size distribution. For the range of operating conditions used, the mean diameter ranged from approximately 4 to 6 mm.

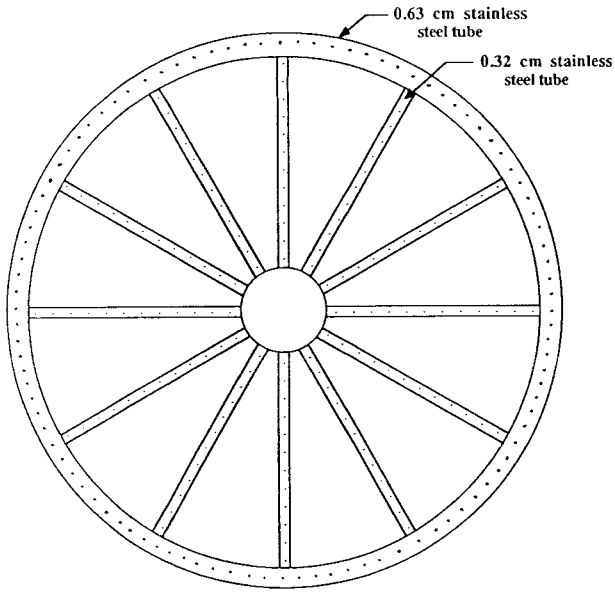

Figure 4. Ring sparger configuration.

The ring is 16.5 cm in diameter; each hole is 0.0033 cm in diameter. Each spoke has 11 holes and the ring has 96 (228 total).

Liquid-phase measurements

Local liquid velocity measurements were obtained via hot-film anemometry using the two-phase flow analysis of Delhaye (1969). Following the technique of Goodman and Sogin (1971), a conical hot-film probe (TSI Inc., Model 1231W) was calibrated in liquid pipe flow of a known velocity. The probe was then placed in the two-phase environment with the axis of the conical film parallel to the riser axis. Digitized probe readings were accumulated in the memory of an Apple IIe microcomputer using a 12-bit analog-to-digital converter. For each sampling port, the probe measurements were made at each of 11 equally-spaced positions across the diameter to generate velocity profiles.

Readings were taken for a period of approximately one minute per location (approximately 500–1,500 readings total) to average temporal fluctuations in the flow. Voltage readings obtained when the gas phase engulfed the sensor were below the liquid-phase calibration curve voltage range, due to markedly reduced heat loss. Delhaye's technique basically consists of separating the gas and liquid readings based on relative magnitude and assuming that single-phase calibration curve remains valid for the airlift liquid-phase readings. The distribution of liquid velocities obtained in the above manner was then used to compute a number-weighted mean local velocity $\bar{v}_l$, and the percent relative liquid turbulence intensity I using the following formulas:

$$\bar{v}_l = \Sigma v_i (N_i - N_o) \tag{1}$$

$$I = \frac{100}{\bar{v}_l} \sqrt{\frac{\Sigma (v_i - \bar{v}_l)^2 (N_i - N_o)}{\Sigma (N_i - N_o)}} \tag{2}$$

where

v_i = instantaneous velocity measurement
N_i = number of velocities v_i in data set
N_o = number of background counts

For a given gas sparging rate, local liquid-phase recirculation in the riser was noticeably higher for the small downcomer configuration than for the corresponding large downcomer case. Although visual observation suggested this interpretation, this conclusion was based primarily on the thermal anemometer response. Based on mass balance closure, the anemometer readings consistently overestimated the axial velocity component in the small downcomer case, indicating an increased random local fluid motion. The increased radial and azimuthal velocity components of the flow increased probe cooling without a commensurate increase in the bulk liquid flow rate, leading to errors in average liquid-phase mass flux measurements. This problem was mitigated substantially by fitting the probe with a 1-in.-dia. (25-mm) cylindrical shield that decreased the tangential velocity components reaching the sensor.

Liquid-phase pressure measurements were made with precision-inclined manometers having a range of 0–150 cm of H_2O. Eight pressure taps (0.24-cm-diameter) were distributed along the riser axis in 22.3-cm increments, allowing generation of axial profiles of liquid-phase pressure.

Gas-phase measurements

Gas or void fraction measurements involved two complementary techniques: gamma densitometry and resistivity probe measurements. Over the last two decades, the principle of gamma radiation attenuation has become a common tool for average void fraction measurements (Schrock, 1969; Delhaye and Jones, 1976; Chan and Banerjee, 1981). Basically, a collimated beam of gamma or X-ray radiation is passed through a two-phase flow channel. The extent to which the beam is attenuated depends directly on the amount of mass in its path. For a binary system with known attenuation coefficients for each phase, the relative quantities for each phase may be computed. A track-mounted, single-beam gamma densitometer was used to scan the length of the riser, providing cross-sectionally averaged void fraction ($\bar{\epsilon}$) measurements as a function of axial position.

A 30-mCi source of Cs-137 was employed as the gamma radiation source; primary photons emitted by the cesium gave the proper balance between transmission and sensitivity for the relatively large 19-cm-diameter riser. Radiation counting was conducted over a single, long-time interval to minimize errors due to statistical fluctuations in the source decay rate. However, since radiation attenuation is a nonlinear phenomenon, this approach introduced an error due to the constant fluctuation of the instantaneous void fraction during the counting period. Quantitative analyses of this error have been attempted by Wyman and Harms (1985) and Barrett (1975). For the low void fraction conditions of this study, the error introduced by the time dependence of the void fraction was estimated to be on the order of 2%.

In addition to providing the axial dependence of $\bar{\epsilon}$, the gamma densitometer measurements were used as a calibration standard for a resistivity probe apparatus. Resistivity probes detect the electrical resistivity difference between gases and liquids. The local, time-averaged void fraction can be measured with these probes by dividing the recorded time, during which the probe is surrounded by gas, by the total sampling time. Due to finite probe drying times in aqueous applications, the transition of the probe voltage between phase values is not instantaneous. A voltage threshold or phase transition level must be deter-

Table 1. Gas-Phase Mass Balance Closure*

Downcomer Size (cm)	Measurement Technique or % Error	Superficial Gas Velocity & Axial Riser Position							
		0.96 cm/s		2.1 cm/s		4.7 cm/s		8.2/8.4 cm/s	
		Lower	Upper	Lower	Upper	Lower	Upper	Lower	Upper
14	Rotameter	290	310	630	670	1,400	1,500	2,470	2,630
	Probe	300	320	660	740	1,320	1,620	2,650	2,750
	% Error	5.2	3.8	4.8	10	6.3	8.3	7.2	4.6
8.9	Rotameter	290	310	630	670	1,400	1,500	2,490	2,650
	Probe	350	350	700	680	1,540	1,510	3,000	2,990
	% Error	21	13	11	1.5	9.7	0.7	21	13

*The tabulated quantity is volumetric gas flow rate (cm^3/s). The error is the deviation of the probe measurement from the meter measurement.

mined to define the boundary between gas- vs. liquid-phase readings. This threshold was set such that the integral of $\epsilon(r)$ equaled $\bar{\epsilon}$, as determined by gamma densitometry for the same axial position.

In addition to radial profiles of void fraction, the radial variation in local gas velocity was measured via resistivity probe techniques. A dual probe featuring two axially displaced platinum electrodes was constructed. Serizawa et al. (1975) used this configuration to measure the transit time of individual bubbles between probe tips. Two different techniques may be used to reduce the acquired data that provide the mean local transit time. The cross-correlation approach may be employed to analyze the two voltage responses of the probe. This method yields the most probable transit time, which for most cases of interest is very close to the mean value. Alternatively, if individual transit-times are accumulated during data acquisition, the resulting spectrum of times may be used to compute a weighted mean value and to examine the variance of times for a given measurement. The latter technique was used in this study. As with the anemometry, data acquisition was microcomputer-based, employing an interface board developed for this research. Any change in probe voltage which exceeded the adjustable threshold was interpreted as a change in phase at the probe tip. Such a change caused an interrupt in an assembly-language-driven program; the interrupt request was serviced by reading the time generated via a crystal oscillator and reenabling interrupts. The final result of this process was a digital time history of the phase environment of the probes. The time resolution was limited to 100 μs due to constraints of the Apple IIe microprocessor speed. This time period constituted less than 2% of the minimum transit time observed.

Error estimates

Each of the individual measurement techniques had possible error associated with it. Some of the sources of error may be readily quantified while others may not. For example, although the anemometry calibration was highly reproducible, the bias introduced due to differences in liquid-phase turbulence is not known quantitatively. The gamma densitometer measurement error was estimated to be on the order of a few percent, as previously noted. Serizawa et al. (1975) reported an estimated error of less than 3% in local void fraction measurements using resistivity probes. Sources of error included distortion of the bubble geometry and velocity due to interaction with the probe tip and the degree to which the probe surface will wet.

The accumulated measurement error for this study was estimated using mass balances. For the gas, the volume flux based on the integrated local void and gas velocity profiles was compared to the gas influx measured by flowmeter and corrected to the pressure at the measurement port. As shown in Table 1, the percent deviation of the integrated flux from the rotameter measurement ranged from 4.6 to 10% for the 14-cm configuration and from 1.5 to 21% for the 8.9-cm case. The higher error range for the smaller downcomer configuration was attributed to increased local recirculation, as previously discussed. For the liquid-phase mass balance, the downcomer velocity profiles were assumed to have negligible error since the flow was one-phase and had modest turbulence, thus rendering it much closer to the calibration conditions than the case for the riser flow. Liquid flux through the riser was calculated by integration of the local profiles and associated void fraction data. The liquid measurement error is reported in Table 2. Again, the maximum error is greater for the small downcomer case due to greater local recirculation. The error range for the large downcomer configuration was 4.5 to 10%, whereas the analogous result for the 8.9-cm downcomer was 8.8 to 21%. The overall error determined for this study compared closely with the two-phase flow measurements of Mou-

Table 2. Liquid-Phase Mass Balance Closure*

Downcomer Size (cm)	Measurement Technique or % Error	Superficial Gas Velocity & Axial Riser Position							
		0.96 cm/s		2.1 cm/s		4.7 cm/s		8.2/8.4 cm/s	
		Lower	Upper	Lower	Upper	Lower	Upper	Lower	Upper
14	Downcomer	7,390	7,390	9,300	9,300	11,740	11,740	15,520	15,520
	Riser	7,040	7,100	9,950	10,260	12,350	12,200	17,060	17,140
	% Error	4.7	3.9	7.0	10	5.2	3.8	9.9	10
8.9	Downcomer	3,750	3,750	5,350	5,350	7,330	7,330	8,370	8,370
	Riser	4,500	4,430	5,820	5,950	8,260	8,340	10,120	9,980
	% Error	20	18	8.9	11	13	14	21	19

*The tabulated quantity is volumetric liquid flow rate (cm^3/s). The error is the deviation of the riser measurement from the downcomer measurement.

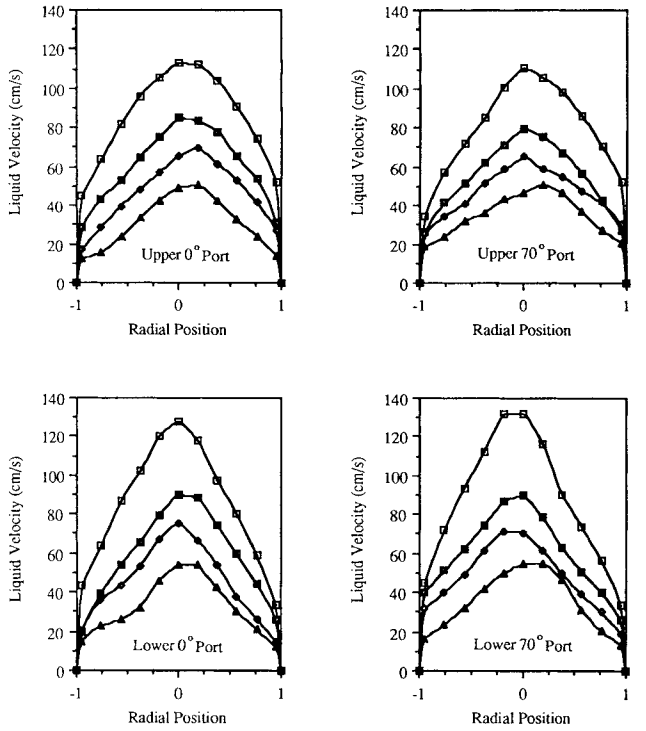

Figure 5. Riser liquid velocity with 14-cm downcomer.

Parameter is superficial gas velocity with values of 8.2, 4.7, 2.1 and 0.96 cm/s from the top curve down.

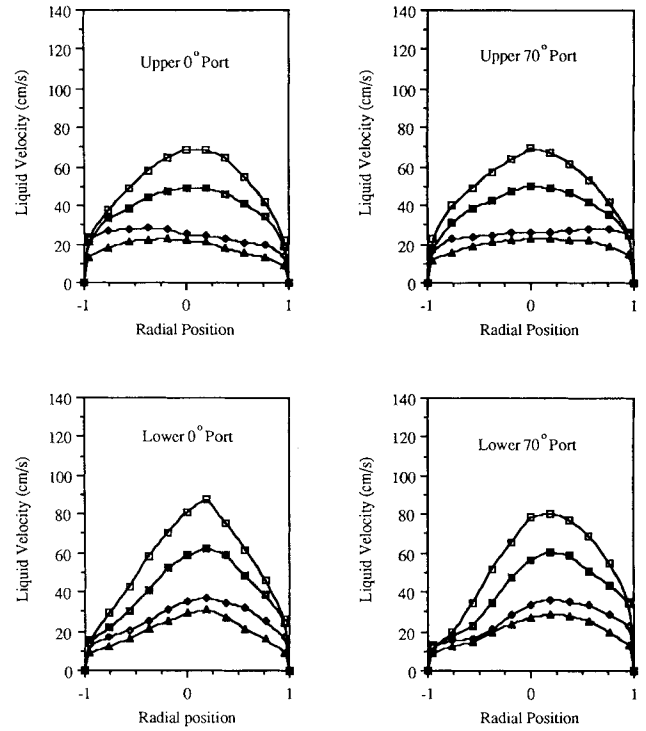

Figure 6. Riser liquid velocity with 8.9-cm downcomer.

Parameter is superficial velocity with values of 8.4, 4.7, 2.1 and 0.96 cm/s from top curve down.

jaes and Dougall (1987), which were obtained using a similar collection of techniques applied to well-developed flow at a small scale.

Results and Discussion of Experiment

Liquid velocity and pressure

Liquid velocity profiles for the four different combinations of azimuthal and axial position in the riser are displayed in Figures 5 and 6. Azimuthal positions that were parallel to the gamma densitometer beam are labeled as the 0° ports; those which were rotated from the gamma beam orientation are denoted as the 70° ports. For a given spatial position and sparging rate, liquid velocities were higher for the large downcomer configuration. Centerline (maximum) riser velocities ranged from approximately 50 to 130 cm/s for the 14-cm downcomer and from 30 to 90 cm/s for the 8.9-cm downcomer. As shown in Figure 7, the downcomer velocity was much higher for the small downcomer. However, the velocity increase was not sufficient to offset the simultaneous decrease in cross-sectional flow area, and lower riser velocities resulted. A comparison of the eight different combinations of downcomer size, and axial and azimuthal position shown in Figures 5 and 6 indicates that the flow was relatively symmetrical with respect to radial and azimuthal position. The velocity profiles broadened noticeably as the flow proceeded along the riser from the

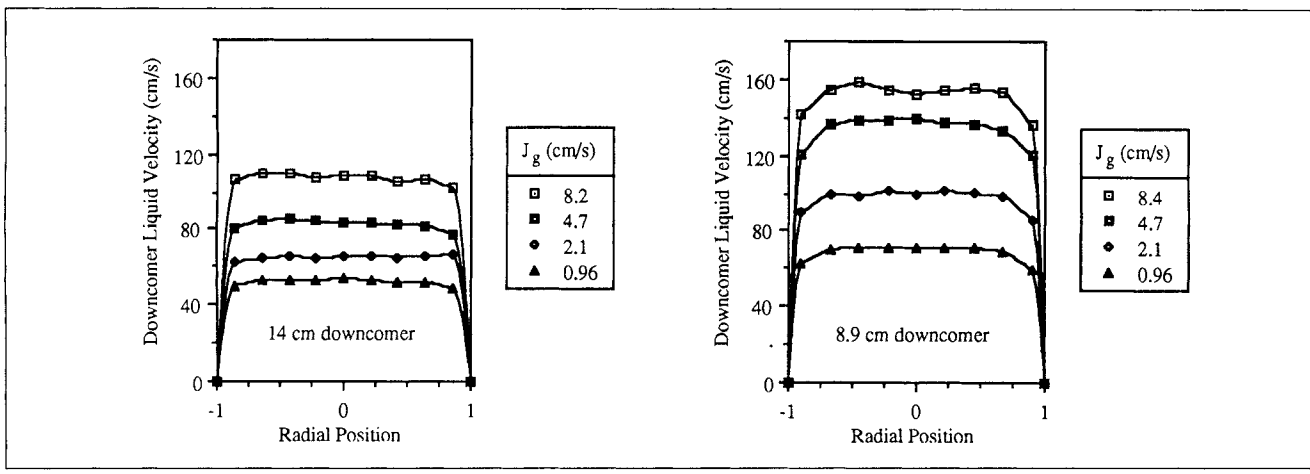

Figure 7. Downcomer liquid velocity at various gas superficial velocities.

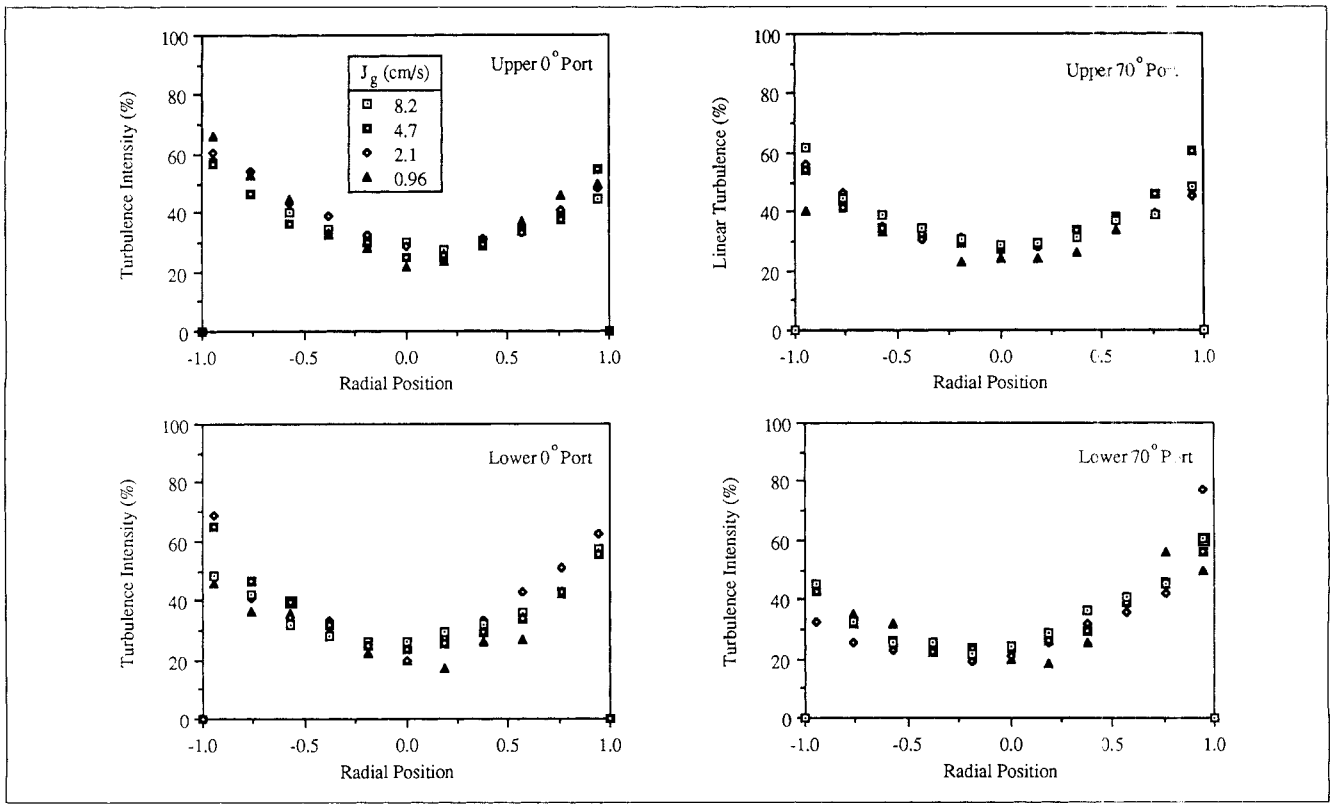

Figure 8. Riser liquid turbulence with 14-cm downcomer.

lower to upper ports. Asymmetries that were present initially tended to diminish. These changes are indicative of developing flow, which is characteristic of airlift risers.

Liquid turbulence levels are shown in Figures 8 to 10, which expressed the turbulence intensity as a percent of the mean local velocity. The relative turbulence intensity was found to be nearly independent of sparging rate as well as azimuthal and axial position. The somewhat reduced turbulence levels detected for the large downcomer configuration were due presumably to decreased local recirculation as compared to the small downcomer case, in which liquid flux was reduced. For all conditions in the riser, the range of turbulence in the two-phase environment was substantially larger than that in the single-phase downcomer flow, e.g., centerline values of 20 to 30% for the two-phase environment vs. 5 to 7% for the single-phase downcomer flow shown in Figure 10. Basing the Reynolds number on the superficial liquid velocity ($Re \equiv DQ_l\rho/A\mu$), the Reynolds numbers for the riser and downcomer varied by a factor of 1.36 for the 14-cm case and by 2.13 for the 8.9-cm case. For the range of operating conditions used, the downcomer Re varied from 5.4×10^4 to 1.41×10^5; the analogous range for the riser was from 2.52×10^4 to 1.04×10^5. The differences in Re were judged to be insufficient to explain the large difference in turbulence intensity between the riser and downcomer. Hence, this difference was attributed primarily to the wakes formed behind bubbles in the two-phase region.

Liquid-phase pressure measurements were made relative to the hydrostatic pressure at a given axial position, i.e., the manometer reading was zero prior to commencement of sparging. Two effects combine to create the pressure change: the change in average density as the single phase becomes the two phase and the development of a velocity head. Upon sparging, the pressure drop was substantially greater for the small downcomer configuration, as reflected in Figure 11. Since the riser velocities with the small downcomer were lower and the void fraction will be shown to be higher, one may conclude that density change makes the greater contribution. Neither effect is large in an absolute sense, as evidenced by the modest scale of the pressure drop in centimeters of water.

Gas velocity and volume fraction

Cross-sectionally averaged void fraction measurements determined with the gamma densitometer are reported in Figure 12. The predictably strong dependence of void fraction upon sparging rate is evident. The axial dependence is modest. Most of the axial dependence is attributable to hydrostatic pressure effects. (The pressure changes upon sparging given in Figure 11 indicate the maximum decrease from hydrostatic pressure to be only 1.5%, and hence this effect is negligible with respect to gas-phase volume changes.) For taller, production-scale reactors, the variation in void fraction due to such hydrostatic effects could be substantial.

The smaller downcomer configuration resulted in notably higher void fraction levels, especially at the higher gas flows. This was primarily a function of the lower liquid-phase velocities in the riser. Since at steady-state the gas-phase velocity roughly equals a constant plus the liquid-phase velocity, the riser gas velocity is also reduced for the small downcomer case. Consequently, the residence time of the bubbles is increased, and the gas holdup is increased relative to the larger downcomer configuration. Local gas fraction measurements are reported

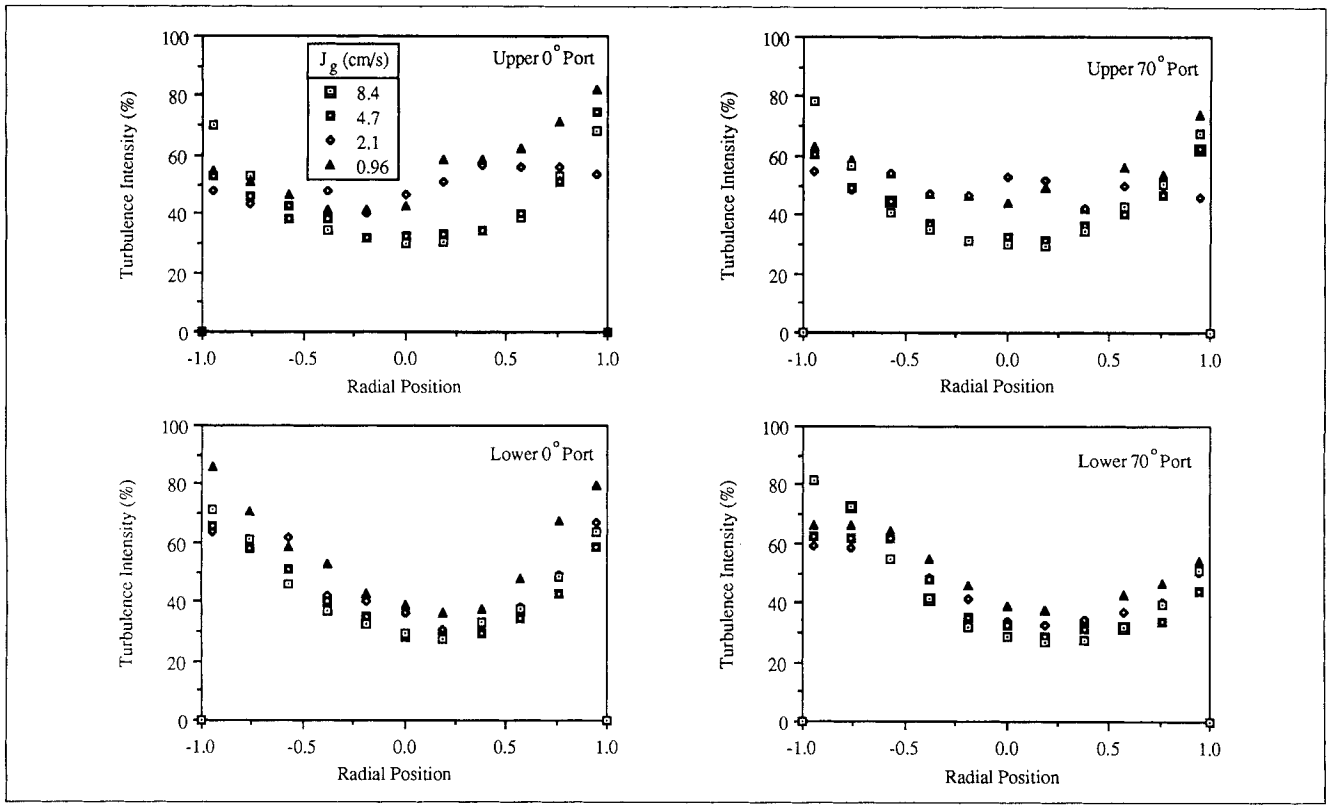

Figure 9. Riser liquid turbulence with 8.9-cm downcomer.

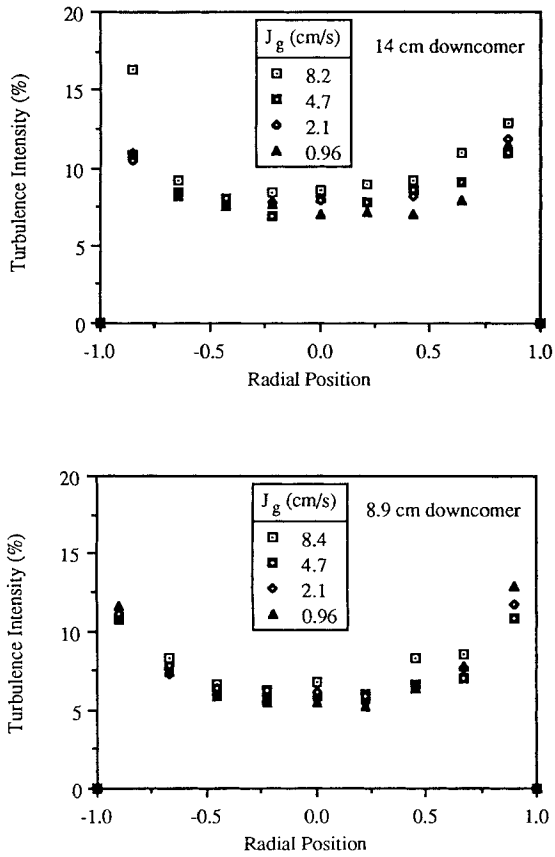

Figure 10. Downcomer liquid turbulence.

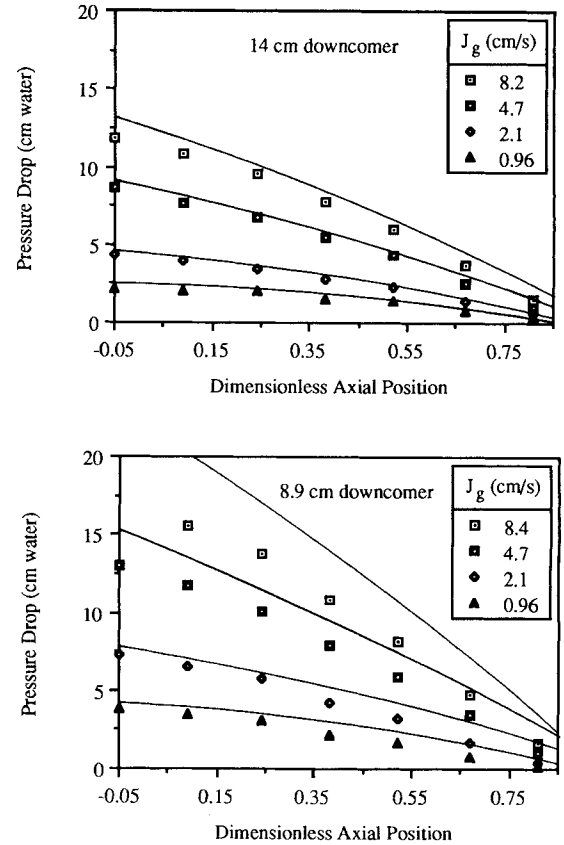

Figure 11. Riser differential liquid pressure drop.

Pressure change is relative to the hydrostatic pressure. Model results represented by solid lines.

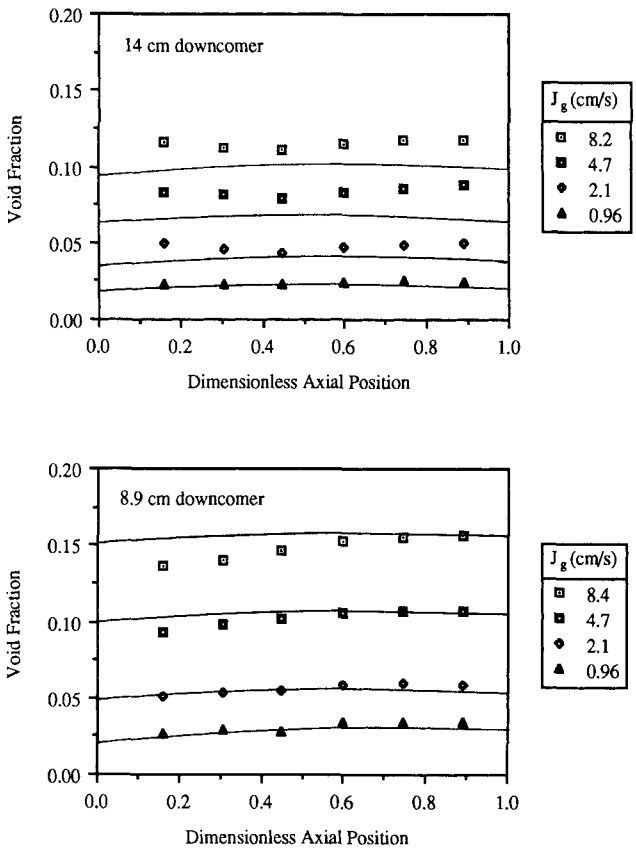

Figure 12. Riser cross-sectionally-averaged void fraction.

Model results represented by solid lines.

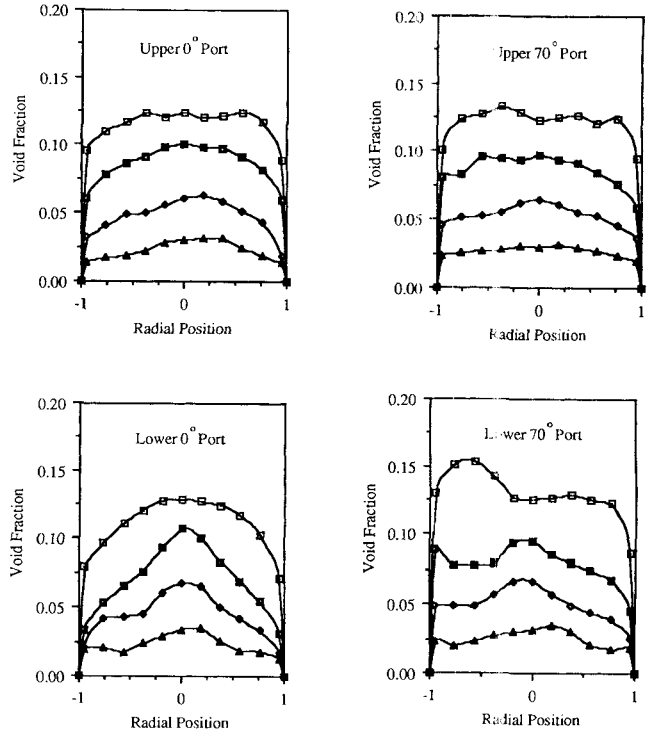

Figure 13. Riser local void fraction with 14-cm downcomer.

Parameter is superficial gas velocity with values of 8.2, 4.7, 2.1 and 0.96 cm/s from top curve down.

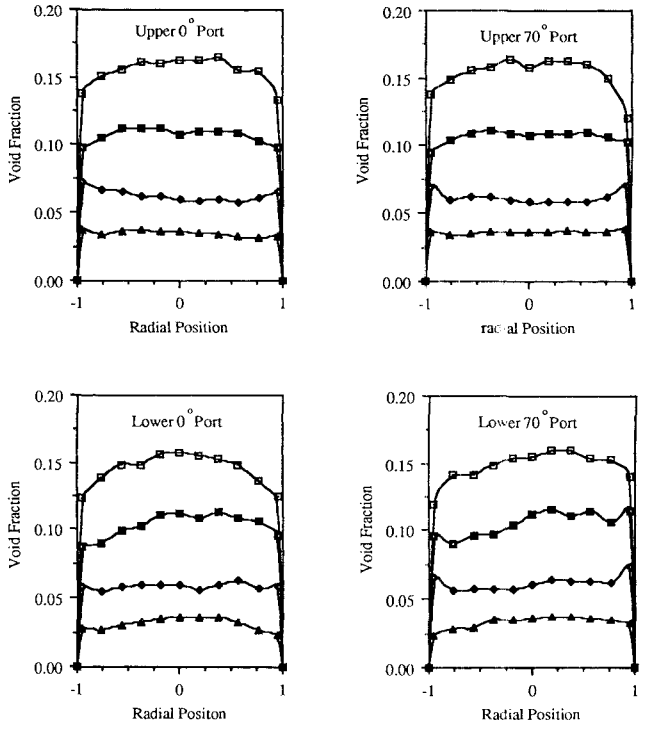

Figure 14. Riser local void fraction with 8.9-cm downcomer.

Parameter is superficial gas velocity with values of 8.4, 4.7, 2.1 and 0.96 cm/s from top curve down.

in Figures 13 and 14. Comparison of changes in both radial and azimuthal positions indicates a rough symmetry for the flow, considering the distinctly asymmetrical nature of the returning liquid flow approximately a meter below the lower port. The relative proximity to the sparger was discernible in the shape of the radial distribution. The distribution of gas occurring at the sparger was determined by the specific design features of the reactor, e.g., the downcomer-to-riser area ratio, the sparger design, and the sparging rate. With the 14-cm downcomer, the void fraction profile was distinctly more peaked at the centerline near the sparger. As the flow moved axially, the void fraction profiles broadened. Near the riser exit, void fraction distributions were almost radially independent for operation with either downcomer. Hence, the developing nature of the flow was readily observable in the void fraction data.

Although the liquid-phase velocity profiles were also observed to broaden near the riser exit (Figures 5 and 6), a much more pronounced radial dependence remained for the liquid velocity, when compared to the exit radial void fraction profile. The strong radial dependence of the riser gas velocity is documented by the resistivity probe measurements summarized in Figures 15 and 16. The functionality here was similar to that of the liquid velocity spatial dependence in that the radial dependence was quite pronounced near the sparger and decreased with axial position. The azimuthal dependence was small. Continuity considerations directly link the void and gas

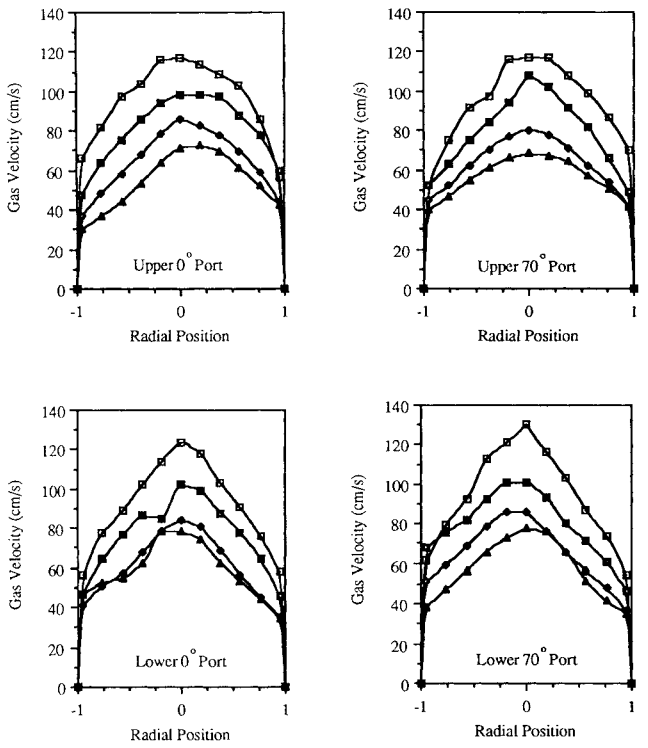

Figure 15. Riser gas velocity with 14-cm downcomer.

Parameter is superficial gas velocity with values of 8.2, 4.7, 2.1 and 0.96 cm/s from top curve down.

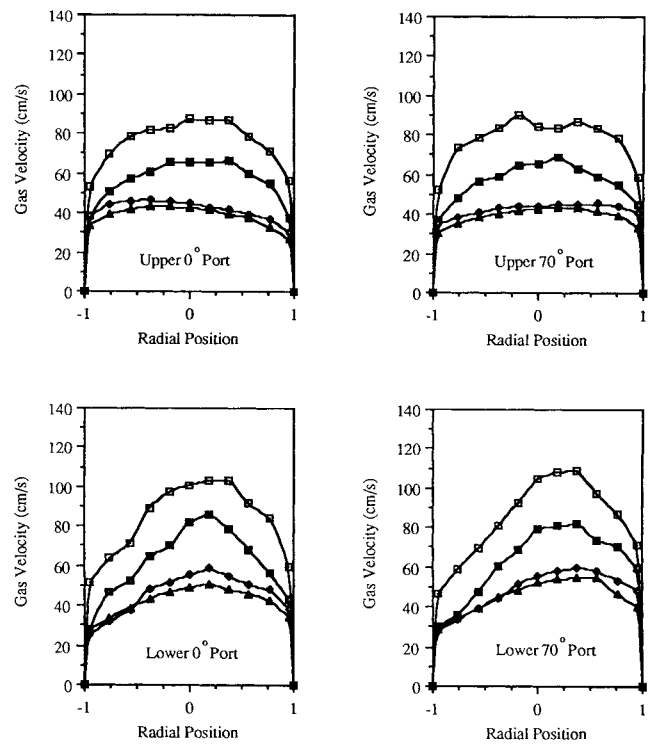

Figure 16. Riser gas velocity with 8.9-cm downcomer.

Parameter is superficial gas velocity with values of 8.4, 4.7, 2.1 and 0.96 cm/s from top curve down.

velocity profiles. This interdependence was clearly observable for the two lowest sparging rates. As the gas flux doubled from 0.96 to 2.1 cm/s, the void fraction roughly doubled as well. Consequently, the gas velocity stayed nearly constant. Additional increases in sparging rate resulted in balanced increases in both void fraction and gas velocity.

Gas-liquid slip velocity

Further insight into local two-phase interactions may be gained by examination of the local slip velocity, defined as the difference between the local gas and liquid velocities. Generally, the slip velocity was roughly constant at approximately 20 cm/s for a wide range of sparging rates, spatial positions and either downcomer configuration, as shown in Figures 17 and 18. An important exception occurred at the highest sparging rate for the 14-cm downcomer case. Near the sparger, the slip velocity decreased to zero or below. Small negative values resulted from the imprecision of the measurements; the extent of overlap of the velocity curves is well within the estimated measurement error. This reduced slip probably is a result of the acceleration of the liquid phase for these operating conditions. As the degassed liquid returned to the two-phase region, the flow channel effectively contracted due to the introduction of the gas phase. The liquid velocity consequently increased. When a gas bubble is introduced into a stagnant liquid, it rapidly accelerates to the terminal velocity characteristic for the physical system. Ordinarily the distance over which this acceleration occurs is small relative to other length scales involved in the process.

However, when both the bubble and the liquid are accelerating as in the present situation, the time required to reach

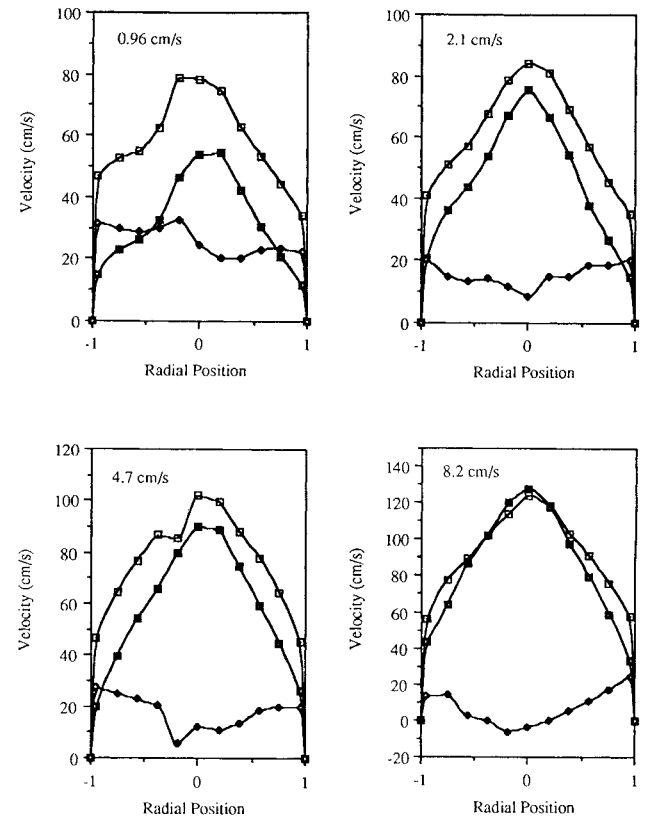

Figure 17. Riser slip velocity for 14-cm downcomer and lower 0° port.

□, gas velocity; ■, liquid velocity; ◆, slip velocity

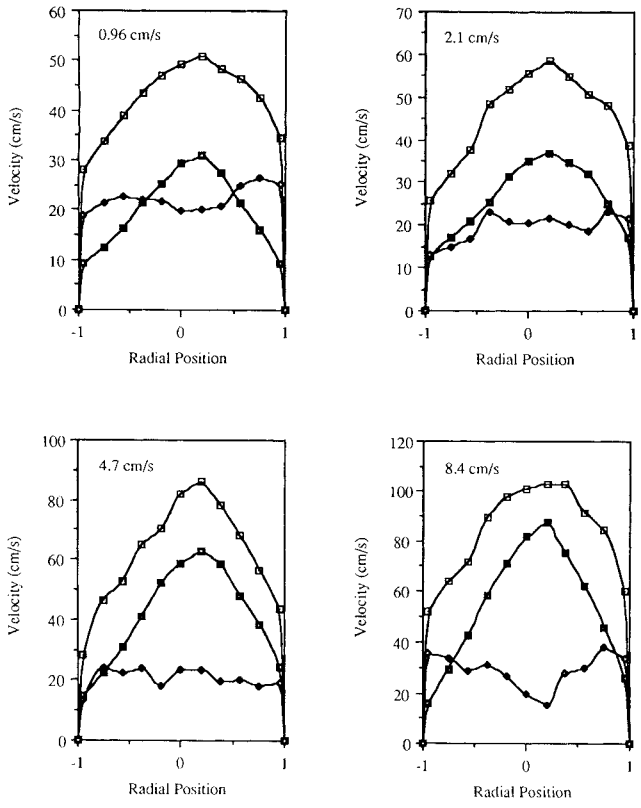

Figure 18. Riser slip velocity for 8.9-cm downcomer and lower 0° port.

□, gas velocity; ■, liquid velocity; ◆, slip velocity

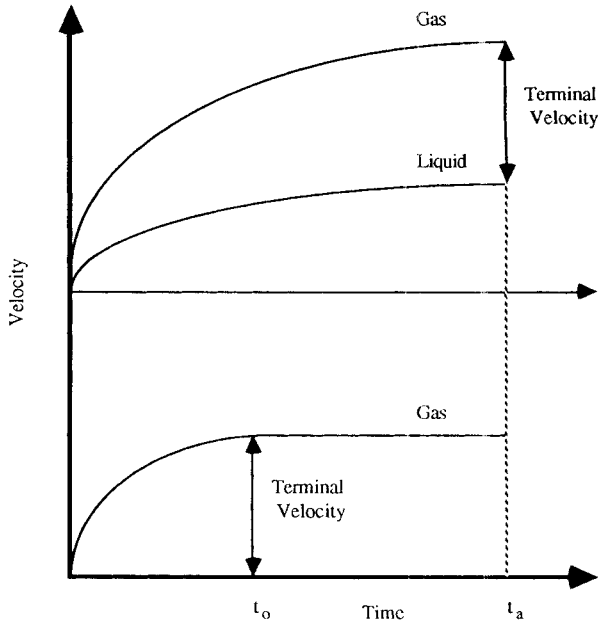

Figure 19. Influence of accelerating liquid flow on the time to reach terminal bubble velocity.

terminal bubble velocity may be increased significantly. This time increment is qualitatively represented in Figure 19 as the difference between t_a and t_o. Under the conditions of high liquid flux and high gas fraction, the zone over which the acceleration occurred extended beyond the midpoint of the reactor; this was true for the case cited above. If profiles had been measured for several other axial positions closer to the sparger, one might expect to see the same phenomenon occurring over a progressively shorter distance from the sparger as the gas flux was decreased. This observed decrease in slip velocity for significant portions of the riser length has implications for gas/liquid mass transfer. More correlations for mass transfer from bubbles to a liquid assume that the liquid side is limiting and that the relative velocity between phases is constant, in this case equal to the slip velocity (Sherwood et al., 1975). The assumed velocity difference does not exist for the acceleration zone, which for certain operating conditions may be a substantial fraction of the two-phase region. The correlations would predict the diffusion-limited mass transfer rate in these regions. Additionally, two-phase flow models which assume a constant slip velocity in their formulation are inherently limited in describing these effects. Although the incorporation of such acceleration effects is beyond the current state of two-phase flow modeling, the limitations of the simpler models should be noted.

Drift-flux model analysis

Both Siegel et al. (1986) and Verlaan et al. (1986) utilized the drift-flux theory of Zuber and Findlay (1965) to analyze airlift hydrodynamics. Drift-flux theory is a one-dimensional analysis derived from mass balances on each of the two phases. The influences of two-dimensional velocity and void fraction profiles enter into the model via the distribution parameter C_o, which is defined as:

$$C_o \equiv \frac{\frac{1}{A}\int_A \epsilon j dA}{\frac{1}{A}\int_A \epsilon dA \frac{1}{A}\int_A j dA} \equiv \frac{\langle \epsilon j \rangle}{\langle \epsilon \rangle \langle j \rangle} \tag{3}$$

where the brackets $\langle\ \rangle$ denote the area average and j is the mixture superficial velocity, i.e., $j = (j_g + j_l)$. If either the void fraction or the velocity profiles are radially uniform, the distribution parameter C_o will equal one. This distribution parameter is used to relate the superficial mixture velocity to the weighted mean gas velocity $\bar{v}_g$ as follows:

$$\bar{v}_g \equiv \frac{\langle \epsilon v_g \rangle}{\langle \epsilon \rangle} = \frac{\langle j_g \rangle}{\langle \epsilon \rangle} = C_o \langle j \rangle + \frac{\langle \epsilon v_{gj} \rangle}{\langle \epsilon \rangle} \tag{4}$$

where v_{gj} is the gas velocity relative to the mixture superficial velocity. In their airlift reactor study, Siegel et al. (1986) computed C_o to be 1.11 by linear regression analysis of average data for $\langle j_g \rangle / \langle \epsilon \rangle$ and $\langle j \rangle$. Similarly, Verlaan et al. (1986) assumed a value of 1.06 based on findings of several related flow studies. Values of C_o computed using the local data of this study are listed in Table 3. For each combination of sparging rate, downcomer size and axial position, C_o was determined using the four pairs of profiles for ϵ and v_g from 0 to R, i.e., two pairs for the 0° port and two for the 70° port. The fact that C_o is near unity in magnitude should not be misinterpreted as indicating that plug flow prevails in the riser, as some in-

Table 3. Drift-Flux Parameters Calculated From Local Data

Axial Location	J_g (cm/s)	14-cm Downcomer				8.9-cm Downcomer			
		C_o*	C_o**	m	n	C_o*	C_o**	m	n
Lower	0.96	1.16	1.09	1.41	1.10	1.10	1.05	1.66	1.83
	2.1	1.14	1.12	1.40	1.35	1.08	1.01	1.98	0.32
	4.7	1.14	1.09	1.73	1.21	1.12	1.02	1.77	1.28
	8.2/8.4	1.10	1.06	1.78	2.38	1.10	1.03	1.89	2.30
Upper	0.96	1.15	1.08	1.88	2.11	1.08	1.01	2.66	0.63
	2.1	1.13	1.08	1.64	1.57	1.08	1.00	2.72	−0.18
	4.7	1.11	1.05	1.83	1.75	1.08	1.01	2.48	1.52
	8.2/8.4	1.10	1.02	2.08	2.21	1.10	1.02	2.27	1.91
Both	Mean	1.13	1.07	1.72	1.69	1.09	1.02	2.18	1.20
	Std. Dev. (%)	0.02	0.03	0.13	0.28	0.01	0.02	0.19	0.72

*Computed using Eq. 3
**Computed using Eq. 7

vestigators have assumed. The magnitude of the distribution parameter is due primarily to the uniformity of the void distributions rather than the character of the phase velocity profiles. This distinction is not obvious when C_o is derived from average data, and it underscores a limitation of the drift-flux model approach. Nevertheless, the values of C_o determined from both average and local data are in good agreement.

Zuber and Findlay (1965) proposed the following forms for the radial dependence of local superficial mixture velocity j and void fraction ϵ:

$$\frac{j}{j_c} = 1 - \left(\frac{r}{R}\right)^m \tag{5}$$

$$\frac{\epsilon - \epsilon_w}{\epsilon_c - \epsilon_w} = 1 - \left(\frac{r}{R}\right)^n \tag{6}$$

where the subscripts c and w refer to center and wall, respectively, and R is the duct radius. In their analysis, Verlaan et al. (1986) adopted the values of $m = 2$ and $n = 7$. In the present study, these parameters were computed directly by fitting profiles of the above form to the local data. Referring to Table 3, m had an average value of 1.72 and a relative standard deviation of 0.13 for the 14-cm downcomer case. The analogous values for the 8.9-cm downcomer case were 2.18 and 0.19. The void fraction profile parameter n was found to have mean and relative standard deviation values of 1.69/0.28 and 1.2/0.72 for the 14 and 8.9 cm cases, respectively. Figures 20 and 21 illustrate how successfully the forms of Eqs. 5 and 6 represent the data. In both figures, the (a) graph is indicative of the best fit encountered in computing the values of Table 3; the (b) graph indicates the poorest fit.

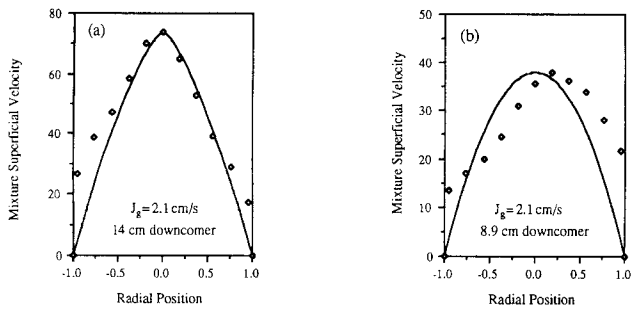

Figure 20. Representative fit of Eq. 5 to data.

The solid lines represent the equation. The discrete points are the average of the lower 0° and 70° port profiles.

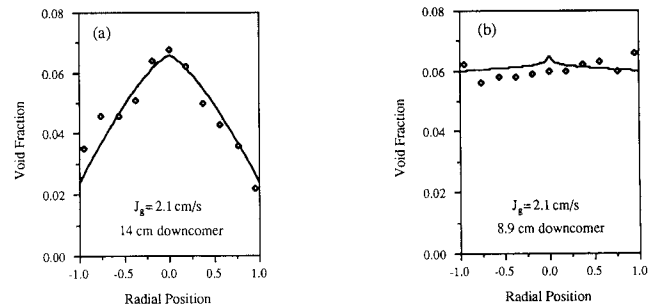

Figure 21. Representative fit of Eq. 6 to data.

The solid lines represent the equation. The discrete points are the average of the lower 0° and 70° port profiles.

When our computed value of m is compared with the value of $m = 2$ assumed by Verlaan et al. (1986), the latter is clearly reasonable. Although our computed n values differ significantly from the value used by Verlaan et al., several points should be noted. Unlike the velocity form, the expression used for void profiles allows a nonzero value at the wall to be used. Accordingly, we determined that nonzero values of ϵ_w were from the data by extrapolation and used them in the present determination of n. Hence, although the void profiles are in general more uniform than are the velocity profiles, the resulting exponents are of similar magnitude. It is unclear from the discussion of Verlaan et al. whether or not a nonzero wall void fraction was assumed. The velocity profiles are reasonably symmetrical, given the regime of developing two-phase flow common to all airlift risers. However, the deviation from perfect symmetry is sufficient to introduce significant uncertainty in the fitted parameters. As reflected in the large relative standard deviations, m and n may vary substantially while continuing to generate an almost equally good fit of the data. Indeed, one computed value of n was negative.

The two sets of C_o values listed in Table 3 were computed in different ways. Using the definition of the distribution parameter given in Eq. 3, one value was determined directly from the radial profiles of j and ϵ. Alternatively, C_o was obtained from the calculated values of m and n using the formula (Zuber

and Findlay, 1965)

$$C_o=\frac{m+2}{m+n+2}\left[1+\frac{\epsilon_c}{\langle\epsilon\rangle}\left(\frac{n}{m+2}\right)\right] \tag{7}$$

The second approach assures that the values of n, m and C_o are self-consistent; it also averages some of the radial variability in the data before determining C_o. Consequently, the values of C_o listed are somewhat less than those computed directly from the data using Eq. 3.

Model Development

The fundamental modeling equations are derived in this section. The development of the riser equations consists of time averaging the point continuity and momentum equations for the gas and liquid phase, volume averaging these turbulent equations of motion, and then area averaging over the reactor cross-section to create a one-dimensional model. The separator and downcomer flow model employs the liquid-phase continuity and mechanical energy balance equations, which are subjected to time averaging and area averaging. To keep the notation simple, all variables represent time-averaged quantities. The liquid phase velocity v is distinguished from the gas-phase velocity v_g by the use of subscript g. Unsubscripted symbols ρ, P and ϵ represent the liquid density, liquid pressure, and the gas volume fraction, respectively. The general configuration of the reactor is shown in Figure 1. Complete details of reactor construction are reported by Young (1989).

Riser

Both the continuity and momentum equations were applied to each phase to develop the riser equations. The development will be done using the liquid phase and then generalized to the gas phase.

Continuity equations

The time-averaged, steady-state continuity equation has the form:

$$\nabla\cdot\rho v=0. \tag{8}$$

Employing the definition of the volume average for any variable Ψ over some arbitrary averaging volume V_a:

$$\langle\Psi\rangle_a\equiv\frac{1}{V_a}\int_{V_a}\Psi dV, \tag{9}$$

the volume-averaged continuity equation becomes:

$$\frac{1}{V_a}\int_{V_a}[\nabla\cdot(\rho v)]dV=0. \tag{10}$$

The averaging volume includes both gas and liquid. Since the liquid-phase equation is being considered, the limits of integration may be rewritten in terms of the liquid volume V_l, rather than the total volume:

$$\frac{1}{V_a}\int_{V_l}\nabla\cdot(\rho v)dV=0. \tag{11}$$

The spatial-averaging theorem for some liquid vector property a:

$$\int_{V_l}\nabla\cdot a dV=\nabla\cdot\int_{V_l}a dV+\int_{A_{gl}}a\cdot n dA \tag{12}$$

may be applied, where A_{gl} represents the gas-liquid interfacial area. The resulting form of the volume-averaged continuity equation is:

$$\nabla\cdot\langle\rho v\rangle_a+\frac{1}{V_a}\int_{A_{gl}}(\rho v)\cdot n dA=0. \tag{13}$$

The second term on the lefthand side represents the mass flux between gas and liquid. Assuming mass transfer to be negligible, the continuity equation can be written as:

$$\nabla\cdot\langle\rho v\rangle_a=0. \tag{14}$$

The average based on the averaging volume is related to the interstitial (i.e., physical) average in the following manner:

$$\langle\rho\rangle_a=(1-\epsilon)\langle\rho\rangle. \tag{15}$$

Substitution into the continuity equation gives:

$$\nabla\cdot(1-\epsilon)\langle\rho v\rangle=0. \tag{16}$$

To rewrite the average of the product of density and velocity, the quantities of interest may be expressed as the sum of the mean value and a deviation (denoted by a tilde):

$$\rho=\langle\rho\rangle+\tilde{\rho}\ \text{ and }\ v=\langle v\rangle+\tilde{v}. \tag{17}$$

By taking the product of these expressions and averaging the results over the liquid phase, it can be shown that

$$\langle\rho v\rangle=\langle\rho\rangle\langle v\rangle+\langle\tilde{\rho}\tilde{v}\rangle. \tag{18}$$

Note that this simplification is due to the fact that by definition the average of the deviations is zero. By assuming that average values are much greater in magnitude than deviations, the product of deviations becomes negligibly small compared to the product of averages. Hence, the volume-averaged liquid continuity equation may be written as:

$$\frac{\partial}{\partial z}[(1-\epsilon)\langle\rho\rangle\langle v\rangle_z]+\frac{1}{r}\frac{\partial}{\partial r}[r(1-\epsilon)\langle\rho\rangle\langle v\rangle_r]=0. \tag{19}$$

The area average of some fluid property Ψ is defined as:

$$\hat{\Psi}\equiv\frac{1}{A}\int_A\Psi dA, \tag{20}$$

where A is the cross-sectional area of the flow channel. By applying the averaging formula to the continuity equation and observing that $\langle v\rangle_r=0$ at the wall, the radial derivative term equals zero. The density is independent of radial position. The order of differentiation and integration may be reversed and

the density may be removed from the area integral. The volume fraction and velocity may be written as the sum of the area average (denoted by the hat symbol) and deviation (denoted by the breve symbol):

$$(1-\epsilon)=1-\hat{\epsilon}-\breve{\epsilon}$$
$$\langle v\rangle_z=\langle\hat{v}\rangle_z+\langle\breve{v}\rangle_z\,. \tag{21}$$

Substitution into the continuity equation and simplification yield:

$$\frac{d}{dz}[\langle\rho\rangle(1-\hat{\epsilon})\langle\hat{v}\rangle_z]=0. \tag{22}$$

This assumption introduces some error into the model in return for computational simplicity. However, the errors are not large. Based on the local property profiles reported here, the error introduced by omitting the integral of the deviations is estimated to be on the order of 10%.

A parallel development for the gas phase produces a directly analogous result of the form:

$$\frac{d}{dz}[(1-\langle\rho\rangle)\hat{\epsilon}\langle\hat{v}_g\rangle_z]=0. \tag{23}$$

Momentum equations

The time-averaged point equations of motion for incompressible flow have the form (Whitaker, 1968):

$$\rho\left(\frac{\partial v}{\partial t}+v\cdot\nabla v\right)=-\nabla P+\rho g+\nabla\cdot\underline{\tau}^{(T)}. \tag{24}$$

where $\underline{\tau}^{(T)}$ is the sum of the viscous and turbulent stress tensors. Neglecting the convective acceleration and assuming steady-state operation, the volume-averaged momentum equation becomes:

$$\frac{1}{V_a}\int_{V_a}\{-\nabla P+\rho g+\nabla\cdot\underline{\tau}^{(T)}\}dV=0. \tag{25}$$

Applying the spatial averaging theorem to the pressure and stress tensor terms and writing the momentum equation for the liquid phase in terms of the intrinsic phase average yields:

$$-\nabla(1-\epsilon)\langle P\rangle+\frac{1}{V_a}\int_{A_{gl}}(-P\underline{I}+\underline{\tau}^{(T)})\cdot n dA+(1-\epsilon)\langle\rho\rangle g+\nabla\cdot(1-\epsilon)\langle\underline{\tau}\rangle^{(T)}=0, \tag{26}$$

where n is the unit normal at any given point on the surface of the gas-liquid interface. Expanding the volume-averaged stress tensor term results in the form:

$$\nabla\cdot(1-\epsilon)\langle\underline{\tau}\rangle^{(T)}=\nabla\cdot(1-\epsilon)\langle\underline{\tau}\rangle+\nabla\cdot(1-\epsilon)\langle\underline{\tau}^{t}\rangle \tag{27}$$

where

τ = liquid viscous stress tensor $=\mu(\nabla v+\nabla v^T)$
$\langle\tau^t\rangle$ = liquid turbulent stress tensor $=-\langle\overline{\rho v' v'}\rangle$
∇v^T = the transpose of the dyad ∇v

The overbar on $-\langle\overline{\rho v' v'}\rangle$ indicates that the time average was done over the entire product. Volume averaging and applying the spatial averaging theorem to $\underline{\tau}$ yields:

$$\langle\underline{\tau}\rangle=\mu[\nabla\langle v\rangle+\nabla\langle v\rangle^T]+\mu\left[\frac{1}{V_a}\int_{A_{gl}}nvdA+\frac{1}{V_a}\int_{A_{gl}}vndA\right]. \tag{28}$$

Since the liquid velocity v is nearly uniform with respect to the position on the bubble interface and the unit normal vector integrates to zero over the surface, the area integrals are zero and

$$\langle\underline{\tau}\rangle=\mu[\nabla\langle v\rangle+\nabla\langle v\rangle^T]. \tag{29}$$

Writing the volume average of the turbulent stress tensor as $\langle\underline{\tau}^t\rangle=-\langle\overline{\rho v' v'}\rangle$, the equations of motion become:

$$-\nabla(1-\epsilon)\langle P\rangle+\frac{1}{V_a}\int_{A_{gl}}(-P\underline{I}+\underline{\tau}^{(T)})\cdot n dA+(1-\epsilon)\langle\rho\rangle g+\nabla\cdot(1-\epsilon)\mu[\nabla\langle v\rangle+\nabla\langle v\rangle^T]-\nabla\cdot(1-\epsilon)\langle\overline{\rho v' v'}\rangle=0. \tag{30}$$

The remaining area integral term represents the total drag force between gas and liquid phases per unit volume. This quantity may also be expressed in terms of F_b, the average force per unit gas-liquid area:

$$\frac{1}{V}\int_{A_{gl}}(-P\underline{I}+\underline{\tau}^{(T)})\cdot n dA\equiv F_b\left(\frac{3\epsilon}{r_b}\right) \tag{31}$$

where $(3\epsilon/r_b)$ is the gas-liquid interfacial area per unit reactor volume.

To develop the one-dimensional model, the axial component of the momentum equation is taken. Expanding the viscous term gives:

$$\nabla\cdot(1-\epsilon)\mu[\nabla\langle v\rangle+\nabla\langle v\rangle^T]=(1-\epsilon)\mu[\nabla^2\langle v\rangle+\nabla(\nabla\cdot\langle v\rangle)]+\mu[\nabla\langle v\rangle+\nabla\langle v\rangle^T]\cdot\nabla(1-\epsilon). \tag{32}$$

Noting that divergence of the velocity vector is zero and assuming that $\langle v\rangle_z=\langle v\rangle_z$ (r,z only), the axial component of the first term on the righthand side becomes:

$$e_z\cdot(1-\epsilon)\mu[\nabla^2\langle v\rangle]=(1-\epsilon)\mu\left[\frac{1}{r}\frac{\partial}{\partial r}\left(r\frac{\partial\langle v\rangle_z}{\partial r}\right)+\frac{\partial^2\langle v\rangle_z}{\partial z^2}\right] \tag{33}$$

where e_z is the unit vector in the axial direction. Similarly, taking the axial component of the second term of the righthand side yields:

$$e_z\cdot\mu[\nabla\langle v\rangle+\nabla\langle v\rangle^T]\cdot\nabla(1-\epsilon)=-2\mu\left(\frac{\partial\langle v\rangle_z}{\partial z}\frac{\partial\epsilon}{\partial z}\right). \tag{34}$$

Except near the sparger, the quantities $\langle v\rangle_z$ and ϵ change only modestly with axial position. The second derivative of $\langle v\rangle_z$ is expected to be at least as small as its first derivative. However, the change in $\langle v\rangle_z$ with r is considerable. Consequently, axial

derivatives may be considered to be negligible relative to the radial derivative, and the axial component of the viscous term may be expressed approximately as:

$$(1-\epsilon)\mu\left[\frac{1}{r}\frac{\partial}{\partial r}\left(r\frac{\partial\langle v\rangle_z}{\partial r}\right)\right]. \tag{35}$$

For the turbulent stress term, the dot product with e_z has the form of the z component of the divergence of a dyad (Bird et al., 1960):

$$e_z\cdot(\nabla\cdot(1-\epsilon)\langle\overline{\rho v'v'}\rangle)=[\nabla\cdot(1-\epsilon)\langle\overline{\rho v'v'}\rangle]_z=\frac{1}{r}\frac{\partial}{\partial r}(r(1-\epsilon)\cdot\langle\overline{\rho v_r'v_z'}\rangle)+\frac{1}{r}\frac{\partial((1-\epsilon)\langle\overline{\rho v_\theta'v_z'}\rangle)}{\partial\theta}+\frac{\partial((1-\epsilon)\langle\overline{\rho v_z'v_z'}\rangle)}{\partial z}. \tag{36}$$

If the flow is assumed to be symmetrical with respect to azimuthal position, the second term on the righthand side is zero. Further, changes in v_z with axial position are expected to be small, and the z derivative term is assumed to be negligible. Consequently, the axial component of the Reynolds stress term becomes:

$$\frac{1}{r}\frac{\partial}{\partial r}(r(1-\epsilon)\langle\overline{\rho v_r'v_z'}\rangle). \tag{37}$$

The momentum equation in the axial direction can be averaged over the cross-sectional area of the riser to eliminate radial dependencies:

$$-\frac{1}{A}\int_A\left[\frac{\partial}{\partial z}((1-\epsilon)\langle P\rangle)\right]dA-\frac{1}{A}\int_A((1-\epsilon)\langle\rho\rangle g_z)dA+\frac{1}{A}\int_A\left[(1-\epsilon)\mu\left(\frac{1}{r}\frac{\partial}{\partial r}\left(r\frac{\partial\langle v\rangle_z}{\partial r}\right)\right)\right]dA+\frac{1}{A}\int_A\left[\frac{1}{r}\frac{\partial}{\partial r}(r(1-\epsilon)\langle\overline{\rho v_r'v_z'}\rangle)\right]dA+\frac{1}{A}\int_A F_{bz}\left(\frac{3\epsilon}{r_b}\right)dA=0. \tag{38}$$

The pressure is virtually independent of radial position and can be removed from the area integral. Reversing the order of integration and differentiation for the pressure term then gives:

$$-\frac{1}{A}\int_A\left[\frac{\partial}{\partial z}[(1-\epsilon)\langle P\rangle]\right]dA=-\frac{\partial}{\partial z}[\langle P\rangle(1-\hat{\epsilon})]. \tag{39}$$

The gravity term may be evaluated similarly since the density is also independent of radial position. In evaluating the viscous term, the time-averaged gas volume fraction ϵ is written as the sum of the cross-sectional average and its deviation. Substitution into the viscous term results in the expression:

$$\frac{\mu}{\pi R^2}\int_0^{2\pi}\int_0^R(1-\epsilon)\left(\frac{1}{r}\frac{\partial}{\partial r}\left(r\frac{\partial\langle v\rangle_z}{\partial r}\right)\right)rdrd\theta=\frac{2\mu}{R^2}(1-\hat{\epsilon})R\left(\frac{\partial\langle v\rangle_z}{\partial r}\right)\Big|_R-\frac{2\mu}{R^2}\int_0^R\epsilon d\left(r\frac{\partial\langle v\rangle_z}{\partial r}\right). \tag{40}$$

The first term on the righthand side represents the viscous drag at the wall based on gradients in the averaged velocity. The second term is assumed to be negligible based on the relative magnitudes of $(1-\hat{\epsilon})$ and $\breve{\epsilon}$. The turbulent stress term may be integrated to obtain:

$$\frac{1}{\pi R^2}\int_0^{2\pi}\int_0^R\left[\frac{1}{r}\frac{\partial}{\partial r}(r(1-\epsilon)\langle\overline{\rho v_r'v_z'}\rangle\right]rdrd\theta=\frac{2}{R}(1-\epsilon)\langle\overline{\rho v_r'v_z'}\rangle|_R, \tag{41}$$

which represents the turbulent stresses at the wall. The combined viscous and turbulent wall drag may be represented in a traditional friction factor form as:

$$\frac{f_r}{D}\frac{1}{2}\rho\langle\hat{v}\rangle_z^2. \tag{42}$$

Lastly, the interfacial drag term F_{bz} is expressed as the sum of its cross-sectional average and a deviation. Noting that the integral of the deviation over the cross section is zero, the gas-liquid drag force term can be shown to have the form:

$$\frac{3}{Ar_b}\int_A F_{bz}\epsilon dA=\hat{F}_{bz}\frac{3\hat{\epsilon}}{r_b}+\frac{3}{Ar_b}\int_A\breve{F}_{bz}\breve{\epsilon}dA. \tag{43}$$

Assuming that the integral of the product of the deviations is small compared to the product of the averages, the final form of the one-dimensional momentum equation for the liquid is:

$$-\frac{d}{dz}[\langle P\rangle(1-\hat{\epsilon})]-(1-\hat{\epsilon})\langle\rho\rangle g_z-\frac{f_r}{D}\frac{1}{2}\rho\langle\hat{v}\rangle_z^2+\hat{F}_{bz}\frac{3\hat{\epsilon}}{r_b}=0. \tag{44}$$

The derivation of the gas momentum equation is analogous to that of the liquid equation with the following differences:

- There is assumed to be negligible interaction between the gas phase and the wall.
- The volume average based on the liquid phase is replaced by the volume average based on the gas phase, i.e., $\langle\Psi\rangle=\epsilon\langle\Psi\rangle_{gas}$.
- The sign of the gas-liquid drag term is reversed.
- The pressure jump between gas and liquid phases is assumed negligible, and the gas pressure is equated with the liquid pressure.
- The gravity force on the gas is assumed negligible.

The resulting gas-phase momentum equation is:

$$-\frac{d}{dz}(\hat{\epsilon}\langle P\rangle)-\hat{F}_{bz}\left(\frac{3\hat{\epsilon}}{r_b}\right)=0. \tag{45}$$

Separator

The mechanical energy balance was employed to analyze the separator liquid-phase flow. Analysis begins with the time-averaged differential mechanical energy equation for steady flow in a fixed control volume:

$$\int_{A_e}\frac{1}{2}\rho v^2(\boldsymbol{v}\cdot\boldsymbol{n})dA=\int_{A_e}\boldsymbol{v}\cdot(\boldsymbol{n}\cdot\underline{\boldsymbol{T}}^{(T)})dA-\int_{A_e}\rho\phi(\boldsymbol{v}\cdot\boldsymbol{n})dA-\dot{E}_v \tag{46}$$

where

$v = \sqrt{v_r^2 + v_\theta^2 + v_z^2}$

$(\boldsymbol{n} \cdot \underline{\boldsymbol{T}}^{(T)}) = -P\boldsymbol{n} + ([\underline{\tau} + \underline{\tau}^{(t)}] \cdot \boldsymbol{n})$

A_e = cross-sectional flow areas at entrances and exits

$\boldsymbol{n}$ = unit vector outwardly normal to A_e

ϕ = gravitational potential

$\dot{E}_v$ = rate of viscous dissipation

Since the bulk flow at both the riser exit and the downcomer entrance is in the axial direction, the time-averaged radial and azimuthal velocity components are small compared to v_z. Hence, $v_{z_{dc}} \approx \sqrt{v_z^2} = v_z$. In the downcomer, measurements showed that the radial dependence of v_z is weak, and $v_z = v_{z_{dc}}$ to a good approximation. The radial dependence is greater in the riser. By expressing the riser volume-averaged velocity as an area average and a deviation, and assuming that the higher-order terms of the velocity deviation are negligible compared to $\langle v \rangle_z$, the first term in the mechanical energy balance can be shown to have the form:

$$\int_{A_e} \frac{1}{2} \rho v^2 (v \cdot n) dA = \frac{\rho}{2} \hat{v}_{z_{dc}}^3 A_{dc} - \frac{\rho}{2} \langle \hat{v} \rangle_z^3 A_r (1 - \hat{\epsilon}). \quad (47)$$

The second integral in the mechanical energy balance may be expanded by substituting the expression for the total stress vector:

$$\int_{A_e} v \cdot (n \cdot \underline{T}^{(T)}) dA = \int_{A_e} v \cdot (-Pn) dA + \int_{A_e} (v \cdot \underline{\tau} \cdot n) dA + \int_{A_e} (v \cdot \underline{\tau}^{(t)} \cdot n) dA. \quad (48)$$

To a very good approximation, the time-averaged pressure is independent of radial position. The pressure integral term becomes:

$$-\int_{A_e} P(v \cdot n) dA \approx (-P \hat{v}_z A)_{dc} + [\langle P \rangle \langle \hat{v} \rangle_z (1 - \hat{\epsilon}) A]_r. \quad (49)$$

Using index notation, the viscous stress term for the downcomer may be shown to have the form

$$v \cdot \underline{\tau} \cdot n = v_z \left[2\mu \left(\frac{\partial v_z}{\partial z} \right) \right] \quad (50)$$

assuming again that the axial acceleration of the flow is negligible in comparison to the pressure and inertial terms. An analogous treatment holds for the riser term. The turbulent stress term reduces to the form:

$$(v \cdot \tau^{(t)} \cdot n) = v_z \rho l_{zz}^2 \left| \frac{\partial v_z}{\partial z} \right| \left(\frac{\partial v_z}{\partial z} \right) \quad (51)$$

where l_{zz} is the Prandtl mixing length of unknown magnitude. The upper limit of the mixing length may be estimated to be a bubble diameter. Since velocity changes in the z direction are small, the turbulent stress term may also be assumed to be small relative to the P and $\hat{v}_z^3$ terms. Again, an analogous development holds for the riser.

Evaluation the gravity term over the entrance and exit yields:

$$\int_{A_e} \rho \phi (v \cdot n) dA = -\rho \phi \langle \hat{v} \rangle_{zr} A_r (1 - \hat{\epsilon}) + \rho \phi \hat{v}_{z_{dc}} A_{dc}. \quad (52)$$

Substitution of the above terms into the original form of the mechanical energy balance results in the expression:

$$\frac{\rho}{2} \hat{v}_{z_{dc}}^3 A_{dc} - \frac{\rho}{2} \langle \hat{v} \rangle_z^3 A_r (1 - \hat{\epsilon}) = -(P \hat{v}_z A)_{dc} + (\langle P \rangle \langle \hat{v} \rangle_z (1 - \hat{\epsilon}) A)_r + \rho \phi \langle \hat{v} \rangle_{zr} A_r (1 - \hat{\epsilon}) - \rho \phi \hat{v}_{z_{dc}} A_{dc} - \dot{E}_v. \quad (53)$$

By substitution of the continuity relationship:

$$\rho \hat{v}_{z_{dc}} A_{dc} = \rho \langle \hat{v} \rangle_{zr} (1 - \hat{\epsilon}) A_r \quad (54)$$

and division by $\rho g v_{z_{dc}} A_{dc}$ the separator mechanical energy equation becomes:

$$\frac{\hat{v}_{z_{dc}}^2}{2g} \left[1 - \frac{1}{(1 - \hat{\epsilon})^2} \left(\frac{D_{dc}}{D_r} \right)^2 \right] - \frac{\langle \hat{P} \rangle_r - \hat{P}_{dc}}{\rho g} + \frac{\dot{E}_v}{\rho g \hat{v}_{z_{dc}} A_{dc}} = 0. \quad (55)$$

The last term is frequently referred to as the minor head loss term h_m and is represented as the product of a loss factor K times the ratio of characteristic kinetic energy per unit volume to the gravity force per unit volume, i.e., $h_m \equiv K v^2 / 2g$. Using the results of Whitaker (1968), one can estimate the loss factors for expansion into the separation tank and contraction into the downcomer as:

$$K = \left[1 - \left(\frac{D_r}{D_t} \right)^2 \right]^2 \text{ and } K = 0.5, \quad (56)$$

respectively. The quantity D_t is the equivalent diameter of the separation tank, which was set equal to the width of the rectangular tank base. Incorporating the minor loss terms and simplifying the use of the continuity equation, the macroscopic momentum balance for the separation chamber has the final form:

$$\frac{\hat{v}_{z_{dc}}^2}{2g} \left[\frac{3}{2} + \left(\frac{D_{dc}}{(1 - \hat{\epsilon}) D_r} \right)^2 \left(\left[1 - \left(\frac{D_r}{D_t} \right)^2 \right]^2 \left(\frac{D_{dc}}{D_r} \right)^2 - 1 \right) \right] + \frac{\langle \hat{P} \rangle_r - \hat{P}_{dc}}{\rho g} = 0. \quad (57)$$

The liquid-phase continuity equation may be applied to the separation chamber with the following intuitive result equating the influx from the riser and the efflux to the downcomer:

$$\rho (1 - \epsilon)_r \langle v \rangle_{zr} A_r = \rho \hat{v}_{z_{dc}} A_{dc}. \quad (58)$$

Downcomer

For modeling purposes, the downcomer section is defined as the flow channel extending from the separator exit to the sparger (see Figure 1). As previously noted, the downcomer flow is assumed to be all liquid. The mechanical energy balance was applied to the downcomer in a manner analogous to the

separation chamber derivation. Following the same arguments made for the separator and noting the changed orientation of the velocity and unit normal vectors, the three integrals of the differential energy balance can be shown to simplify to the following forms:

$$\int_{A_e}\frac{1}{2}\rho v^2(\boldsymbol{v}\cdot\boldsymbol{n})dA=-\frac{\rho}{2}\hat{v}_{z_{dc}}^3A_{dc}+\frac{\rho}{2}\langle\hat{v}\rangle_{z_r}^3(1-\hat{\epsilon})A_r \quad (59)$$

$$\int_{A_e}\boldsymbol{v}\cdot(\boldsymbol{n}\cdot\underline{\boldsymbol{T}}^{(T)})dA=P_{dc}\hat{v}_{z_{dc}}A_{dc}-\langle P\rangle_r\langle\hat{v}\rangle_{z_r}(1-\hat{\epsilon})A_r \quad (60)$$

$$\int_{A_e}\rho\phi(\boldsymbol{v}\cdot\boldsymbol{n})dA=-\rho\phi_{dc}\hat{v}_{z_{dc}}A_{dc}+\rho\phi_r\langle\hat{v}\rangle_{z_r}(1-\hat{\epsilon})A_r. \quad (61)$$

Collecting terms, the mechanical energy balance becomes

$$\frac{\rho}{2}\langle\hat{v}\rangle_{z_r}^3(1-\hat{\epsilon})A_r-\frac{\rho}{2}\hat{v}_{z_{dc}}^3A_{dc}=P_{dc}\hat{v}_{z_{dc}}A_{dc}-\langle P\rangle_r\langle\hat{v}\rangle_{z_r}(1-\hat{\epsilon})A_r+\rho\phi_{dc}\hat{v}_{z_{dc}}A_{dc}-\rho\phi_r\langle\hat{v}\rangle_{z_r}(1-\hat{\epsilon})A_r-\dot{E}_v. \quad (62)$$

The gravity potential terms may be simplified using the relationship:

$$\phi_{dc}-\phi_r=\int_o^L g\,dz=gL. \quad (63)$$

By incorporating the continuity relationship between the downcomer and riser velocities and dividing by $\rho g\hat{v}_{z_{dc}}A_{dc}$, the downcomer mechanical energy equation takes the form:

$$\frac{\hat{v}_{z_{dc}}^2}{2g}\left[\left(\frac{D_{dc}}{D_r}\right)^2-1\right]=\frac{P_{dc}-\langle P\rangle_r}{\rho g}+L-\frac{\dot{E}_v}{\rho g\hat{v}_{z_{dc}}A_{dc}}. \quad (64)$$

The last term may be represented as the sum of the frictional loss h_f and the minor losses h_m. The frictional losses are commonly written in the form of the Darcy-Weisbach formula (Whitaker, 1968)

$$h_f=f_{dc}\left(\frac{L}{D}\right)_{dc}\frac{\hat{v}_{z_{dc}}^2}{2g}. \quad (65)$$

The minor losses may be depicted using K loss factors as before. Whitaker (1968) lists the following values:

K(90° elbow with miter) = 1.3

K(expansion from downcomer to riser) $=\left[1-\left(\frac{D_{dc}}{D_r}\right)^2\right]^2$

K(tee used as ell entering through branch) = 1.5. (66)

Incorporating these empirical expressions, the macroscopic mechanical energy balance for the downcomer has the final form:

$$\frac{\hat{v}_{z_{dc}}^2}{2g}\left[\left(\frac{D_{dc}}{D_r}\right)^2-1\right]+\frac{\langle P\rangle_r-P_{dc}}{\rho g}-L+f_{dc}\left(\frac{L}{D}\right)_{dc}\frac{\hat{v}_{z_{dc}}^2}{2g}+\frac{\hat{v}_{z_{dc}}^2}{2g}\left\{1.3+\left[1-\left(\frac{D_{dc}}{D_r}\right)^2\right]^2\right\}+1.5\frac{\langle\hat{v}\rangle_{z_r}^2}{2g}=0 \quad (67)$$

To solve the system of equations, forms must be found for the three frictional terms, i.e., the two-phase wall drag in the riser, the bubble drag, and the liquid wall drag in the downcomer. The proper selection of these forms will be addressed in turn in the next three sections.

Two-phase frictional effects

Riser Wall Friction. Values for the two-phase friction factor f_r appearing in the riser momentum equation were calculated from the data using a momentum balance. For a section of the riser, the liquid-phase macroscopic momentum balance may be written in the form:

$$[(1-\hat{\epsilon}_2)\langle P\rangle_2-(1-\hat{\epsilon}_1)\langle P\rangle_1]+\rho g(1-\epsilon)L-LF_b\left(\frac{3\epsilon}{r_b}\right)+f_r\left(\frac{1}{2}\rho v^2\right)\left(\frac{L}{D}\right)=0 \quad (68)$$

where the subscripts 1 and 2 refer to the entrance and exit, respectively. The gravity and gas-liquid drag effects have been written using ϵ, the average void for the riser section, but the pressure term retains the local values of the void at the entrance and exit. The average liquid velocity is defined as $v=Q_l/(1-\epsilon)A$. When this equation was used to compute f_r from the data of Young (1989), the resulting values varied widely and erratically in magnitude. Since the pressure is several orders of magnitude greater than any other variables, small measurement errors in local void fraction created unacceptable scatter in the pressure difference terms. Consequently, the equation was rewritten using ϵ in the pressure difference term. The gas macroscopic momentum balance was written in the same manner, and the resulting forms are:

$$\epsilon[\langle P\rangle_2-\langle P\rangle_1]+\rho_g g\epsilon L+LF_b\left(\frac{3\epsilon}{r_b}\right)=0$$

$$(1-\epsilon)[\langle P\rangle_2-\langle P\rangle_1]+\rho g(1-\epsilon)L-LF_b\left(\frac{3\epsilon}{r_b}\right)+f_r\left(\frac{1}{2}\rho v^2\right)\left(\frac{L}{D}\right)=0 \quad (69)$$

Adding the gas and liquid equations and observing that $\rho(1-\epsilon)>>\rho_{gas}\epsilon$ yields the mixture macroscopic momentum equation:

$$[\langle P\rangle_2-\langle P\rangle_1]+\rho g(1-\epsilon)L+f_r\left(\frac{1}{2}\rho v^2\right)\left(\frac{L}{D}\right)=0 \quad (70)$$

The mixture equation was applied between the lower and upper data collection ports, located at approximately the midpoint and top of the riser, respectively. The value of ϵ was the arithmetic average of the local values at the upper and lower ports, as determined from the integrated radial profiles of ϵ. Table 4 lists the computed values of the two-phase friction factor, which fall into the range 0.24–0.50. These two-phase values are at least an order of magnitude greater than the Moody friction factors for the corresponding one-phase liquid flow, a characteristic value for which is 0.02 (Bird et al., 1960).

Table 4. Riser Two-Phase Friction Factors*

Downcomer Size (cm)	J_g (cm/s)	ϵ	$\langle v_l \rangle$ (cm/s)	f_r (Data)	f_r^* (Akita)
14	0.96	0.024	26.6	0.41	0.18
	2.1	0.049	34.3	0.49	0.19
	4.7	0.080	44.8	0.24	0.18
	8.2	0.120	61.7	0.34	0.16
8.9	0.96	0.033	13.6	0.50	0.43
	2.1	0.059	19.9	0.36	0.38
	4.7	0.102	28.6	0.24	0.34
	8.4	0.147	34.4	0.48	0.33

*Computed using correlation of Akita et al. (1988).

Numerous correlations for two-phase friction factors have been presented in the literature. Wallis (1969) discussed several approaches to calculating two-phase frictional effects, but he concluded that for flows of low void fraction, one-phase values were a good approximation. One of the earliest and most widely used correlations was developed by Lockhart and Martinelli (1949). For the flows of interest in this study, Lockhart-Martinelli multipliers increase the single-phase values by approximately 10%, thus significantly underestimating the effects observed in these experiments. Several investigators have developed improvements to the Lockhart-Martinelli approach by considering acceleration effects (Love, 1974), gravity effects (Hughmark, 1963), and systems having a greater range of flow rate and physicochemical properties (Baroczy, 1966; Chisholm, 1966). Even incorporating these improvements by various investigators, the friction factor values for two-phase flow change only minimally from the single-phase values relative to the order of magnitude differences observed experimentally in this study.

In recent years, two-phase frictional correlations which depart from the basic Lockhart-Martinelli approach have also been developed (Lombardi and Pedrocchi, 1972; Beattie, 1973; Davis, 1974). However, these alternative correlations again estimated only modest increases relative to the single-phase values.

Previous studies of airlift hydrodynamics have cited a lack of agreement with common two-phase correlations for frictional effects. Hsu and Dudukovic (1980) calculated two-phase friction factors for an extemal-loop airlift reactor having unusually large aspects ratios of up to 90. For laminar flow conditions, the two-phase values matched those correlated for one-phase liquid flow. However, under turbulent conditions, the experimental values were approximately threefold higher than the analogous single-phase values. Hence, Hsu and Dudukovic developed a new correlation to represent the two-phase wall drag. A similar result was reported by Merchuk and Stein (1981). These researchers employed the conventional Blasius single-phase friction factors but then had to add an "effective length" term, which resulted in frictional effects more than an order of magnitude larger than conventional single-phase head loss factors. Most recently, Akita et al. (1988) reported friction factors for their external-loop reactor based on the study of a variety of liquid phases. They also ascertained that commonly cited two-phase friction factor correlations markedly underpredicted the friction factor values derived from their experiments.

Since the conventional two-phase correlations acceptably represent the frictional drag for the many applications in the chemical and gas industry but clearly do not so represent the wall shear in airlift reactors, some fundamental difference between the two applications must exit. Returning to the basic derivation of the friction factor functionality illuminates this difference. Although the Moody diagram incorporates only the Reynolds number and wall roughness dependencies of the friction factor, the derivation of Bird et al. (1960) indicates a strong dependence upon L/D ratio as well. The majority of two-phase flow studies and applications may safely assume well-developed flow profiles as $L/D >> 1$. This is not the case in most airlift risers, where typical aspect ratios fall in the range of 5 to 20.

Several studies of two-phase flow further underscore the importance of this effect. In their study of the flow structure and distribution effects in two-phase flows, Herringe and Davis (1978) noted that the presence of developing flow effects strongly influences friction factor values. Most friction correlations assume homogeneous flow of the two phases in analyzing the data. Herringe and Davis determined that the failure to account for the nonuniform distribution of the phases across the flow duct also contributed to the underestimation of two-phase friction factors. Pal et al. (1979) developed a friction factor correlation for vertical air/water flow and found values roughly an order of magnitude greater than those of Lockhart-Martinelli. The 5-cm tube used in their study had an L/D ratio of 40. Although the authors did not explicitly consider entrance length effects in their analysis, it is likely that developing flow in the relatively short tube significantly contributed to the higher than anticipated drag forces. Further discussion of the limitations of the common two-phase friction factor correlations was given by Friedel (1980), who concluded that large errors are due in part to inadequacies of void fraction measurement and resulting errors in the calculation of the static pressure change.

The entrance length pressure drop for two-phase flow has yet to be explicitly researched. However, for well-developed flow, mixtures having small volume fractions of gas have been shown to have wall friction effects that are only moderately greater than the analogous single-phase case. Hence, analysis of single-phase entrance length effects should provide general insight into the expected two-phase behavior. Several analyses of laminar developing flow have been conducted. The theoretically more complex turbulent case has yet to be rigorously addressed, but some researchers have published analyses which attempt to extrapolate from the laminar to the turbulent case.

Lundgren et al. (1964) estimated the loss coefficient due to flow development under laminar conditions. After simplification using the continuity equation, the momentum equation was cross-sectionally averaged and integrated axially from the entrance ($z=0$) to the point at which flow was fully developed ($z=\zeta$). The form of the resulting pressure drop is:

$$\frac{P_o - P}{1/2\rho U^2} = f\frac{\zeta}{D} + k(\zeta). \tag{71}$$

where

f = friction factor for developed flow
U = (uniform) velocity profile at channel entrance
D = pipe diameter
$k(\zeta)$ = additional pressure drop due to developing flow effects

The kinetic energy contribution of $k(\zeta)$ has the form:

$$2\left[\frac{1}{A}\int\left(\frac{u(\zeta)}{U}\right)^2 dA - 1\right]. \tag{72}$$

The viscous component of $k(\zeta)$ depends on local values of the developing flow profile $u(r,z)$. Lundgren et al. developed an equivalent form for this viscous component which is based on the final developed profile $u(\zeta)$ only. In the course of this development, the nonlinear convective acceleration term was linearized by substituting $\alpha U\partial u/\partial z$ for $u\partial u/\partial z$ where α is a weighting factor. The value of α was determined by equating analogous forms for $k(\zeta)$ derived from the momentum balance and from a parallel treatment of the mechanical energy balance. The resulting form for the excess pressure drop in laminar flow is:

$$k(\zeta)=\frac{2}{A}\int\left[\left(\frac{u_\infty(r)}{U}\right)^3-\left(\frac{u_\infty(r)}{U}\right)^2\right]dA, \tag{73}$$

where A is the cross-sectional area of the flow channel. For circular tubes, the laminar flow loss coefficient was found to be 1.33. Separating the sources of the total loss showed that the coefficient for momentum change (kinetic energy) losses was 1.00 and for frictional losses in excess of the developed flow case was 0.33. Agreement between the theoretical values and published experimental data was good. Singh et al. (1980) argued that the approach of Lundgren et al. could be generalized to apply to the developing turbulent flow case, although the validity of this assumption was not demonstrated. By assuming that the developed profile conforms to the 1/7 power case, Singh et al. estimated the additional loss coefficient to be 0.076.

Thus, the theoretical analyses support the existence of significantly higher pressure drops under developing flow conditions, in qualitative agreement with the present study. Quantitative comparison between these theoretical analyses and the empirical results discussed here is limited by differences in the flow conditions. Lundgren et al. addressed single-phase, laminar flow in a horizontal pipe, whereas airlift risers operate in two-phase, turbulent vertical flow. Although Singh et al. applied Lundgren's result directly to turbulent flow, a thorough analysis would likely indicate that important terms involving the Reynolds stresses were ignored. Further, the magnitude of the momentum change component of $k(\zeta)$ would clearly be increased in the airlift case, due to the acceleration of the liquid phase upon entering the two-phase region.

Friction factors derived from the current study agree with those recently reported by Akita et al. (1988) to within a factor of two or better, as shown in Table 4. Akita et al. developed their correlation based on the data taken in an external-loop airlift reactor using four different liquids of varying physicochemical properties. The superficial gas velocities employed were in the range of 0 to 20 cm/s. In light of the lack of similar correlations in the general multiphase flow literature, Akita's correlation was adopted to represent wall friction effects in the riser section for the current model. As reported by Akita and coworkers, the wall friction factor has the form:

$$f^*=0.0468\left(\frac{\sqrt{gD_r}}{U_l}\right)^{1.1}\sqrt{\epsilon} \tag{74}$$

where U_l represents the superficial liquid velocity. As shown in the following expressions for the wall shear stress, the riser friction factor f_r in this study differs from Akita's f^* by a factor of four and is based solely on the liquid phase rather than the mixture:

$$\begin{aligned}\tau_{\text{wall}}&=f_r\left(\frac{1}{2}\rho v_l^2\right)\left(\frac{1}{4}\right)\\ \tau_{\text{wall}}&=f^*\left(\frac{1}{2}\rho v_l^2\right)(1-\epsilon)\end{aligned} \tag{75}$$

Therefore, $f_r=4f^*(1-\epsilon)$. Accounting for these differences and incorporating constant values for g and D_r yield the final expression:

$$f_r=41.6\left(\frac{\sqrt{\epsilon}}{\langle v\rangle^{1.1}(1-\epsilon)^{0.1}}\right) \tag{76}$$

Gas-Liquid Drag Force. The interfacial drag effects between gas bubbles and the surrounding liquid have been studied from a range of perspectives. In the simplest laminar case, the bubble is assumed to be spherical and a modified Stoke's law analysis is applied while permitting slip at the interface. Numerous extensions to this base case have been offered (Zick and Homsy, 1982; Gal-Or and Waslo, 1968; Brinkman, 1949; Ranz, 1952; and Hasimoto, 1959). However, the turbulent flow case applicable to airlift risers is not amenable to theoretical analysis. Empirical drag force coefficients for turbulent flow around individual hard spheres are in routine use. Ishii and Zuber (1979) critiqued and extended these turbulent correlations to apply to a swarm of fluid particles. It has been shown that in all but the most closely controlled environments, sufficient contaminants are present on the bubble surface to markedly reduce the slip between gas and liquid (Griffith, 1960; Ishii and Pei, 1980). Hence, the fluid bubbles act much like rigid particles on the surface, and the magnitude of the drag force is similar to the classical solid sphere value. Additionally, for the relatively low bubble concentrations prevailing in airlift risers, the drag coefficients developed by Ishii and Zuber are similar in magnitude to the single-particle case. The drag correlation adopted from Ishii and Zuber for the airlift model has the following form:

$$C_D=\frac{4r_b}{3}\sqrt{\frac{g\Delta\rho}{\sigma}}(1-\epsilon)^{-1/2} \tag{77}$$

where r_b is the bubble radius and σ is the interfacial surface tension. The correlation applies to swarms of distorted fluid particles, in which the viscosity of the continuous phase greatly exceeds that of the discrete phase. The total drag force on one bubble F_D is given by:

$$F_D=-C_D\frac{1}{2}\rho\langle v\rangle|\langle v\rangle|A_d \tag{78}$$

where A_d is the projected area of the bubble. Converting to a form for drag per unit bubble area F_b and employing the relative velocity gives:

$$F_b = \frac{r_b}{6}\left(\frac{g\rho^3}{\sigma(1-\epsilon)}\right)^{\frac{1}{2}} |\langle v_g\rangle - \langle v\rangle| (\langle v_g\rangle - \langle v\rangle) \qquad (79)$$

Note that when this expression is substituted into the momentum equations, the explicit dependence upon the bubble radius disappears. An implicit dependence remains due to the fact that the drag force expression assumes a certain range of particle shapes and sizes.

Downcomer Wall Friction Factor. The wall frictional effects in the downcomer are also expected to be influenced by entrance length phenomena. The measured velocity profiles in the downcomer show a much smaller radial dependence than the accelerating two-phase flow near the sparger. Hence, the relative contribution of the momentum changes to the overall pressure drop is expected to be less. To calculate the downcomer frictional losses Δh_f, the following form of the liquid-phase mechanical energy balance was applied between the downcomer entrance and the sparger location:

$$\frac{v_{dc}^2}{2g}\left[\left(\frac{D_{dc}}{D_r}\right)^2 - 1\right] + \frac{\langle P\rangle_s - P_{dc_t}}{\rho g} - L + \Delta h_f + \Delta h_m \qquad (80)$$

where as before the frictional and minor losses are correlated using the forms:

$$\Delta h_m = \frac{v_{dc}^2}{2g}\left(1.3 + \left[1 + \left(\frac{D_{dc}}{D_r}\right)^2\right]^2\right) + 1.5\frac{\langle v\rangle^2}{2g} \qquad (81)$$

$$\Delta h_f = f_{dc}\left(\frac{L}{D}\right)_{dc}\frac{v_{dc}^2}{2g}. \qquad (82)$$

The resulting values are shown in Table 5. These observed friction factors indicate a two- to threefold increase in magnitude compared to the Moody correlation. The exact values were roughly dependent on the L/D ratio. In the absence of published correlations for developing flow friction factors, the following constant values derived from the data were utilized:

$$f_{dc}(14 \text{ cm downcomer}) = 0.06$$
$$f_{dc}(8.9 \text{ cm downcomer}) = 0.04 \qquad (83)$$

Simplification of separator and mechanical energy equation

As noted previously, the clear liquid depth in the separation chamber was set at twice the riser diameter to maximize the liquid flow rate and minimize gas-phase recirculation. The hydrodynamics of this region may be approximated as being well mixed. Consequently, the pressures at any point along the bottom of the separator should be equal to a close approximation. This qualitative result is reflected quantitatively in the separator mechanical energy balance:

$$\frac{v_{dc}^2}{2g}\left[\frac{3}{2} + \left(\frac{D_{dc}}{(1-\hat{\epsilon})D_r}\right)^2\left(-1 + \left[1 - \left(\frac{D_r}{D_t}\right)^2\right]^2\left(\frac{D_{dc}}{D_r}\right)^2\right)\right] + \frac{\langle P\rangle_t - P_{dc_t}}{\rho g} = 0. \qquad (84)$$

Table 5. Downcomer Liquid-Phase Friction Factors

J_g	14-cm downcomer				8.9-cm downcomer			
(cm/s)	Δh_{1-s}^*	Δh_m	Δh_f	f_{dc}	Δh_{1-s}^*	Δh_m	Δh_f	f_{dc}
0.96	−3.0	2.3	0.7	0.047	−5.6	3.6	2.0	0.046
2.1	−5.6	3.6	2.0	0.074	−10.9	7.5	3.4	0.040
4.6	−10.7	5.8	4.9	0.115	−19.8	14.0	5.8	0.037
8.4	−15.5	10.1	5.4	0.039	−24.3	18.3	6.0	0.029

*Sum of the first three terms in the downcomer mechanical energy balance equation; units are cm of H_2O

Using as representative the case of the larger diameter downcomer and $\epsilon = 0.05$, the first term reduces to $4.76 \times 10^{-4} v_{dc}^2$. For a characteristic liquid velocity of 100 cm/s, the difference between the pressure heads at the riser exit and downcomer entrance is approximately 4.76 cm H_2O. Since the absolute pressure head is on the order of 10^4 cm H_2O, the two pressures may be approximated as being equal. Further, the pressure is assumed to be hydrostatic. Hence, the separator mechanical energy balance simplifies to the form

$$\langle P\rangle_t = P_{dc_t} = \rho g h_t \qquad (85)$$

Model solution approach

Four ordinary differential equations describe the riser hydrodynamics. Substitution of the simplified separator mechanical energy equation into the downcomer expression leaves two algebraic equations describing the flow through the separator and downcomer. The riser equations must be integrated along the column. The resulting values at the riser entrance and exit are then substituted into the algebraic equations and consistency between the two sections is checked.

The boundary conditions for the riser equations are written at the exit from the riser since the pressure is known there. Hence, the boundary conditions are as follows:

Liquid Continuity:	$z = L$	$(1-\hat{\epsilon})\rho\langle v\rangle \dot{L}$
Gas Continuity:	$z = L$	$(\hat{\epsilon}\langle v_g\rangle\langle P\rangle M)/(RT) = \dot{G}$
Liquid Momentum:	$z = L$	$\langle P\rangle = \rho g h_t + P_{atm}$
Gas Momentum:	$z = L$	$\left(\frac{d\hat{\epsilon}}{dz}\right)_t = 0$ (86)

where

L = distance from the sparger to the separator
$\dot{L}$ = liquid mass flux
$\dot{G}$ = gas mass flux
h_t = depth of liquid in the separator
P_{atm} = atmospheric pressure
$(d\hat{\epsilon}/dz)_t$ = axial change in gas volume fraction at the top of the riser

The continuity equations can be readily integrated to provide algebraic relationships relating the phase velocities to the mass fluxes. Substitution into the momentum equations results in two coupled equations for the two unknowns $\langle P\rangle$ and ϵ. From the experimental analysis, it is known that the axial dependence of the void fraction is weak, particularly near the top of the

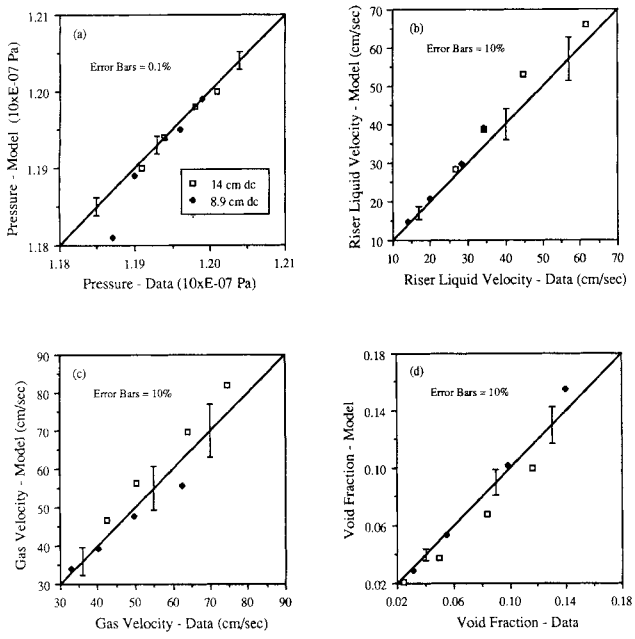

Figure 22. Experimental data vs. model predictions.

riser. Therefore, the boundary condition of $(d\epsilon/dz)_t = 0$ is reasonable. Writing the momentum equations at the exit results in two nonlinear algebraic equations in ϵ_t and $(d\langle P\rangle/dz)_t$:

$$-(1-\hat{\epsilon}_t)\left(\frac{d\langle P\rangle}{dz}\right)_t - \rho(1-\hat{\epsilon}_t)g + F_b\left(\frac{3\hat{\epsilon}_t}{r_b}\right) - \frac{f_r}{D}\frac{\rho}{2}\left(\frac{\dot{L}}{(1-\hat{\epsilon}_t)}\right)^2 = 0$$

$$-\hat{\epsilon}_t\left(\frac{d\langle P\rangle}{dz}\right)_t - F_b\left(\frac{3\hat{\epsilon}_t}{r_b}\right) = 0 \qquad (87)$$

The quantity $\dot{L}$ is not known *a priori* and must be estimated to initiate computation. When a value is assigned to $\dot{L}$, the above algebraic equations may be solved by Newton-Raphson iteration to give the corresponding value of ϵ_t at the boundary.

The momentum equations may be integrated down the column using a simple Runge-Kutta technique. The calculated values of the pressure at the sparger $\langle P\rangle_s$ and gas fraction at the sparger ϵ_s may be substituted into the downcomer mechanical energy balance to compute a new value of $\dot{L}$. A new guess for $\dot{L}$ may be derived from the old guess and the newly computed value by simple linear weighting. The process may be repeated until convergence is achieved. This algorithm was employed in the model solution.

Results and Discussion of Modeling

Model comparison to current empirical study

The model was solved for each set of conditions used in the experimental phase of this work. The computed vs. measured values of the pressure, liquid and gas riser velocities, and void fraction are summarized in Figure 22. The predicted and measured pressures are compared at the level of the sparger. For all of the variables, comparison is made at the midpoint of the riser. The solid 45° line represents exact agreement between theory and experiment. Since the absolute magnitude of the pressure is orders of magnitude greater than any of the other terms, the pressure differences must be predicted within a very close tolerance. Accordingly, in Figure 22a the error bars indicate a 0.1% deviation of the computed pressure vs. measured values for the two different downcomer sizes and four sparging rates. For all other figures, the error bars indicate a 10% deviation. The relative error ranges from 0 to 22% in magnitude; this corresponds closely to the range of error in mass balance closure computed for the empirical results.

The axial dependence of the pressure and void fraction is also predicted by the model. Comparison between theory and experiment for the pressure change is given in Figure 11. The discrete values represent experimental results, and the solid curves depict model results. The pressure change is defined as the difference in pressure between the conditions of zero gas flow and some given sparging rate. Both the velocity of the fluid and the change in fluid density upon sparging contribute to the measured pressure change. Void fraction as a function of axial position is displayed in Figure 12. Again, theory and experiment agree to within at least 22%, and the correct trends are predicted by the model. Consequently, the agreement between the model predictions and the values measured in this study is concluded to be good.

Model comparison to literature study

Merchuk and Stein (1981) conducted one of the most complete experimental studies of airlift hydrodynamics to appear in the literature to date. Their study provides a judicious case for testing the general applicability of the current model. Their reactor was sufficiently similar to that used in this study to permit reasonable comparison, but was sufficiently different to provide a test of the model's generality. Merchuk and Stein employed an external-loop reactor having a 14-cm-diameter riser and downcomer connected to a separation chamber having a free liquid surface. For the case to be compared, a multiorifice sparger was used, and no gas recirculation occurred. These features parallel this study. However, the aspect ratio was over three times greater $[(L/D)_r = 29$ vs. 8], the area ratio of riser to downcomer was greater (1.0 vs. 0.54 and 0.22), and the maximum gas-phase mass flux was significantly higher (0.034 vs. 0.012 g/cm^2·s).

The model was solved for the geometry and operating conditions of Merchuk and Stein's investigation. The correlation for the gas/liquid drag force should be applicable regardless of the changes noted. Although the aspect ratio is increased, the riser for this (and most other) airlift fermentors operates in the developing flow regime. Hence, Akita's correlation for the wall drag should be generally applicable. Similarly, the friction factor of 0.06 determined for the 14-cm downcomer was assumed to hold for the downcomer of Merchuk and Stein.

Merchuk and Stein measured the axial dependence of void fraction using manometric techniques. Figure 23 displays their reported data as well as the curve generated by the model presented here for three sparging rates covering the range used by Merchuk and Stein. Both the trends and overall magnitude agree favorably. Void fraction and liquid velocity measurements as functions of superficial gas velocity appear in Figure 24. Merchuk and Stein measured liquid velocity with an Anubar flow sensor. Measurements were taken at or extrapolated to the midpoint of the riser axis ($z/L = 0.56$). The solid lines are the present model predictions, which again represent the physical phenomena well.

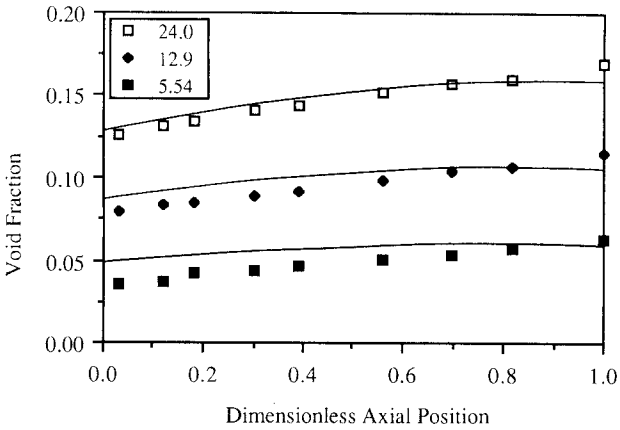

Figure 23. Predicted void fraction vs. measurements of Merchuk and Stein (1981).

Model represented by solid lines. Parameter is gas superficial velocity in cm/s.

Model predictions with change of scale

Design and scale-up are obvious potential applications of the current model. No detailed studies of airlift hydrodynamics in larger-scale reactors have appeared in the literature. Nevertheless, as an illustration of what may be expected to occur with changes of scale in these devices, the differential model was solved for the case of a reactor having an order of magnitude greater liquid volume than the reactor studied. In specifying the large-scale geometry, many important reactor features may be held constant, including $(L/D)_r$, (A_{dc}/A_r) and $(L/D)_{dc}$. Additionally, the depth of nonaerated liquid in the separator was fixed at twice the riser diameter at both scales.

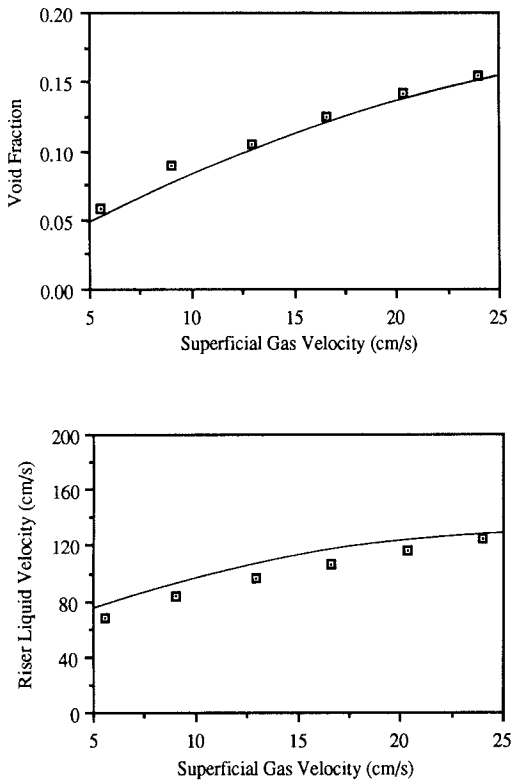

Figure 24. Measurements of Merchuk and Stein (1981) vs. model predictions.

Model represented by solid line.

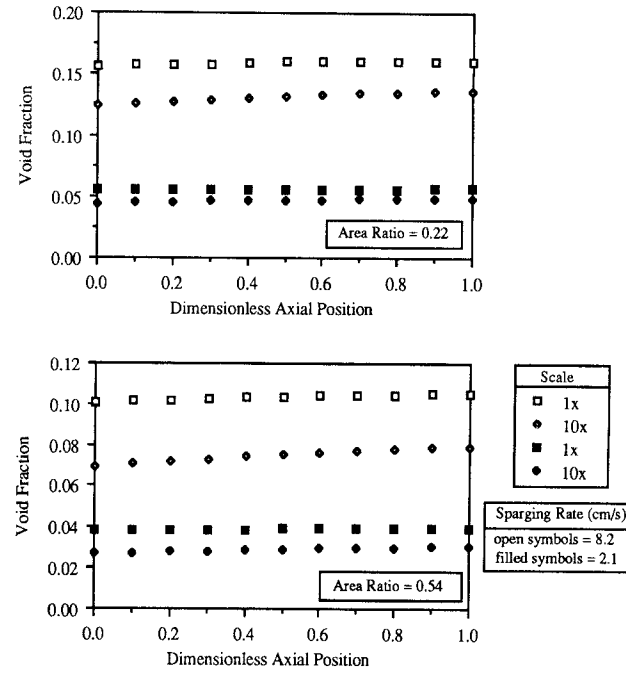

Figure 25. Void fraction dependence on axial position and scale.

All points computed from the model.

In the derivation of the dimensionless model equations (Young, 1989), six dimensionless groups occur in the final form of the model equations. The two groups depending upon geometry only [i.e., $(L/D)_{dc}$ and (D_{dc}/D_r)] were held constant with the scale change. If the same gas and liquid are used and the reactor temperature is unchanged, the term $(R\rho/MP_{\text{ref}})$ does not change with scale. The gravity force term $(g\rho L_r/P_{\text{ref}})$ varies with scale since the reference pressure at the top of the riser P_{ref} changes proportionally much less than the riser length L_r. The term for interfacial drag effects $L_r(g\rho/4\sigma)^{1/2}$ also changes due to its linear dependence upon the riser length. The wall drag correlation term $20.8(L/D)_r(\rho/P_{\text{ref}})^{0.55}$ changes only to the extent that the reference pressure changes. Overall, the changes in the dimensionless groups reflect our intuitive expectation that as scale increases the forces dependent upon volume (i.e., the body force and gas-liquid drag per unit volume) become increasingly important relative to the frictional drag at the walls.

The dependence of void fraction upon axial position for the two scales is portrayed in Figure 25, where the downcomer to riser area has been held constant at 0.54 and at 0.22, respectively. The small-scale reactor always has a higher gas fraction for a given sparging rate (based on gas mass flux). For a given scale, higher void fractions always result in greater phase velocities. However, this generalization does not hold when comparing different scales. As seen in Figure 26, the average phase velocities of the large-scale reactor always exceed the corresponding velocities of the small-scale reactor, even though the void fractions were smaller. In light of the decreasing relative importance of the wall friction with scale-up, greater phase

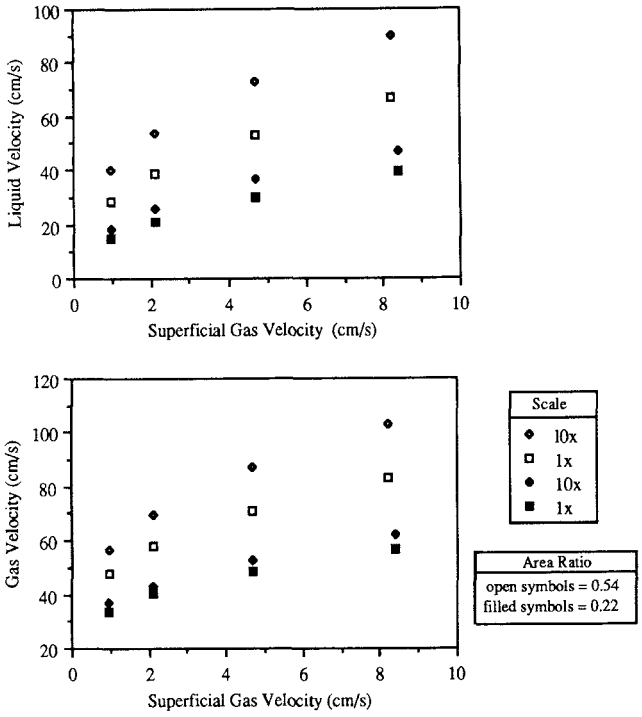

Figure 26. Riser velocity dependence on sparging rate and scale.

All points computed from the model.

velocities are expected. For a given gas mass flux, the void fraction will be less for reactors having greater phase velocities due to decreased mean residence time of the bubbles.

The phase velocities predicted for the two different area ratios also are indicated in Figure 26. The relative change in velocity with scale is much less for the small downcomer case. The second-order velocity dependence of the downcomer wall drag results in a disproportionately greater retardation of liquid circulation for the small downcomer case, where velocities are higher. This effect of different (A_{dc}/A_r) values may be evaluated further by contrasting the experimental results of this study to those of Merchuk and Stein (1981). For the current case of $G = 0.0067$ g/cm^2·s and $(A_{dc}/A_r) = 0.22$, $\epsilon = 0.10$ and $\langle v \rangle = 29$ cm/s. For Merchuk and Stein's reactor operating with a similar gas mass flux of $G = 0.0078$ and $(A_{dc}/A_r) = 1.0$, the void fraction was significantly reduced to $\epsilon = 0.05$. However, liquid velocity was more than twice as great with $\langle v \rangle = 69$ cm/s at the riser midpoint. Hence, the experimental evidence qualitatively supports the model predictions regarding the interaction among the void fraction, the phase velocities and scale changes.

Summary and Conclusions

Local two-phase flow measurements were obtained in a pilot-scale, external-loop airlift bioreactor using two different downcomer sizes. The gas-liquid system was air and water, and the gas phase was not recirculated. Sparging rates, in terms of superficial gas velocity, ranged approximately from 1.0 to 8.0 cm/s, using a multiorifice ring sparger. The axial dependence of the cross-sectionally averaged gas volume fraction was determined using a track-mounted gamma densitometer. Hot-film anemometry was used to measure the radial and azimuthal dependence of the liquid velocity and turbulence intensity for two axial riser locations. The same spatial dependence was ascertained for the gas velocity and volume fraction using dual resistivity probe techniques. The axial distribution of liquid-phase pressure was measured with precision inclined manometers.

The axial dependence of the void fraction was found to be modest, with the majority of the observed increase with axial position being attributed to hydrostatic pressure changes. The radial dependence of the gas and liquid velocities and of the void fraction was substantial, especially near the sparger. Consequently, prior assumptions of plug flow for the gas phase in airlift risers were shown to be incorrect. Drift-flux distribution parameter values previously deduced from averaged data agree reasonably well with values computed directly from local measurements. The proximity of C_o to unity results primarily from the relatively uniform void profiles, rather than from plug flow in the gas phase. Local property changes with azimuthal position were small, and the flow may be characterized as being azimuthally symmetric.

Developing flow effects were pronounced, as evidenced by distinct changes in the radial profiles of fluid flow properties with axial position. Under certain operating conditions, liquid acceleration effects near the sparger resulted in greatly reduced slip velocities in a substantial portion of the riser. Presumably, gas-liquid mass transfer in this region would be reduced significantly under such conditions relative to a fully-developed flow.

A hydrodynamic model was developed directly from the point equations for continuity and motion. This approach allowed all model assumptions to be delineated clearly and created mathematical forms that are suitable for further development involving more complex operating conditions and fluid properties. The riser model is a two-fluid or separated-flow type, allowing phase differences in flow phenomena to be predicted. The model is differential, incorporating changes in fluid flow phenomena with axial position. Macroscopic energy balance equations were used to describe flow effects in the gas separation chamber and in the downcomer. Empirical quantities enter into the model only for frictional effects. No correlations for pressure, void fraction, or phase velocities were used. The riser differential equations were solved using a fourth-order Runge-Kutta technique, beginning at the riser exit and descending to the sparger. The void fraction boundary condition was computed using the approximation that the axial derivative of the void fraction is zero at the riser exit, as demonstrated in the experimental results.

The developing two-phase flow characteristic of airlift risers was observed in this study to create significantly higher frictional effects at the wall than is routinely observed for well-developed flow. This conclusion agrees with the findings of Akita et al. (1988), and Akita's correlation for riser wall friction factors was adopted for use in this study. For the turbulent bubble flow regime observed, the gas-liquid frictional interactions were found to be close in magnitude to the classical values for frictional drag around a single, hard sphere. Ishii and Zuber (1979) generalized the classical drag coefficients to include the case of swarms of fluid particles; the resulting correlation was used in this study.

In the downcomer, the liquid-phase developing flow was found to have increased frictional effects, resulting in friction factors two to three times greater than the analogous well-

developed case. In the absence of literature correlations for developing flow friction factors, averaged empirical values measured in this study were included in the model. Analysis of the separator mechanical energy balance suggested that the liquid pressure in the separation chamber may be approximated as uniform and equal to the hydrostatic pressure. These assumptions were incorporated into the model.

This model was solved using the physical parameters which apply to our experiments and to those for the study of Merchuk and Stein (1981). For both cases, the predicted values agreed well with the respective experimental data, typically to within 10%. The model was also solved for a hypothetical large-scale reactor, having a design analogous to the one used in this study. Differences in void fraction and phase velocities for the two scales were significantly greater for the large downcomer case than for the small downcomer case. Available experimental evidence from the literature qualitatively supports the trends predicted for large-scale reactors.

Notation

A = cross-sectional area of flow channel
C_D = bubble drag coefficient
C_o = drift-flux theory distribution parameter
D = diameter
F_b = drag force per unit gas/liquid interfacial area
F_D = drag force per bubble
f, f^* = friction factors
g = gravitational acceleration
G = gas mass flux
h_t = depth of fluid in the separation tank
I = liquid turbulence intensity
j = superficial mixture velocity
j_g = superficial gas velocity
k = excess pressure drop due to developing flow effects
L = axial distance from sparger to riser
L = liquid mass flux
m,n = exponents defined by Eqs. 5 and 6
M = molecular weight of gas
n = unit normal vector
N_i = number of instantaneous velocity measurements in data set
N_o = number of background counts
P = pressure
Q = volumetric flow rate
r = radial coordinate; radius
R = outer tube radius; gas constant
Re = Reynolds number
t_o = time to reach terminal velocity without liquid acceleration
t_a = time to reach terminal velocity with liquid acceleration
T = temperature
v = fluid velocity
v_{gj} = gas velocity relative to mixture velocity
U = uniform velocity profile at flow channel entrance
z = axial component

Greek letters

α = weighting factor in linearization scheme of Lundgren et al.
ϵ = phase volume fraction
ϵ_g = void or gas fraction
ζ = axial length of flow development zone
θ = azimuthal component
μ = viscosity
ρ = liquid density
σ = gas/liquid interfacial tension
$\underline{\tau}$ = viscous stress tensor

Subscripts

atm = atmospheric
b = bubble
c = center of tube
dc = downcomer
g = gas
gl = gas/liquid interface
l = liquid
r = riser
s = sparger
t = separation tank
w = wall
z = axial coordinate
∞ = beyond the entrance length

Superscripts

t = turbulent
T = transpose
(T) = total

Greek letters

$\overline{\alpha}$ = time average of the quantity α
α' = deviation from time average
$\langle\ \rangle$ = volume average
$\hat{\Psi}$ = area average of ψ
$\check{\Psi}$ = deviation from area average
$\bar{\Psi}$ = deviation from volume average

Literature Cited

Akita, K., T. Okazaki, and H. Koyama, "Gas Holdups and Friction Factors of Gas-Liquid Two-Phase Flow in an Air-Lift Bubble Column," *J. Chem. Eng. Japan*, **21**, 476 (1988).

Barker, T., and J. Wogan, "The Application of Air-Lift Fermenters to the Cultivation of Filamentous Fungi," *Euro. J. Appl. Microbio. Biotech.*, **13**, 77 (1981).

Baroczy, C. J., "A Systematic Correlation for Two-Phase Pressure Drop," *AIChE Symp. Ser.*, **62**(64), 232 (1966).

Barrett, P. R., "Systematic Errors in the Discrete Time Interval Transmission Method for the Estimation of Void Statistics in Boiling Channels," *Nuc. Eng. Design*, **30**, 316 (1975).

Beattie, D. R. H., "A Note on the Calculation of Two-Phase Pressure Losses," *Nuc. Eng. Design*, **25**, 395 (1973).

Bello, R. A., C. W. Robinson, and M. Moo-Young, "Gas Holdup and Overall Volumetric Oxygen Transfer Coefficient in Airlift Contactors," *Biotech. Bioeng.*, **27**, 369 (1985).

Bird, R. B., W. E. Stewart, and E. N. Lightfoot, *Transport Phenomena*, Wiley, New York (1960).

Blenke, H., "Loop Reactors," *Adv. Biochem. Eng.*, **13**, 121 (1979).

Bovonsombut, S., A.-M. Wilhelm, and J.-P. Riba, "Influence of Gas Distributor Design on the Oxygen Transfer Characteristics of an Airlift Fermenter," *J. Chem. Tech. Biotechnol.*, **40**, 167 (1987).

Brinkman, H. C., "A Calculation of the Viscous Force Exerted by a Flowing Fluid on a Dense Swarm of Particles," *Appl. Sci. Res.*, **A1**, 27 (1949).

Chan, A. M. C., and S. Banerjee, "Design Aspects of Gamma Densitometers for Void Fraction Measurements in Small Scale Two-Phase Flows," *Nuc. Inst. Methods*, **190**, 135 (1981).

Chisholm, D., "Pressure Gradients Due to Friction during the Flow of Evaporating Two Phase Mixtures in Smooth Tubes and Channels," *Int. J. Heat Mass Transfer*, **16**, 347 (1973).

Chisti, M. Y., B. Halard, and M. Moo-Young, "Liquid Circulation in Airlift Reactors," *Chem. Eng. Sci.*, **43**, 451 (1988).

Davis, M. R., "The Determination of Wall Friction for Vertical and Horizontal Two-Phase Bubble Flows," *J. Fluids Eng.*, **96**, 173 (1974).

Delhaye, J. M., "Hot-Film Anemometry in Two-Phase Flow," in Two-Phase Flow Instrumentation, from the Eleventh National ASME/AIChE Heat Transfer Conference, Aug. 3-6, Minneapolis, Minn., 58 (1969).

Delhaye, J. M., and O. C. Jones, "Photon-Attenuation Techniques," Argonne National Laboratory Report, **76-75**, 42 (1976).

Fields, P. R., and N. I. H. Slater, "Tracer Dispersion in a Laboratory Air-Lift Reactor," *Chem. Eng. Sci.*, **38**, 647 (1983).

Fields, P. R., and N. I. H. Slater, "The Influence of Fluid Mixing

upon Respiratory Patterns for Extended Growth of a Methylotroph in an Air-Lift Fermenter," *Biotech. Bioeng.*, **25**, 93 (1984).
Fields, P. R., F. R. G. Mitchell, and N. D. H. Slater, "Studies of Mixing in a Concentric Tube Air-Lift Reactor Containing Xanthan Gum by Means of an Improved Flow Follower," *Chem. Eng. Commun.*, **25**, 93 (1984).
Freedman, W., and J. F. Davidson, "Hold-Up and Liquid Circulation in Bubble Columns," *Trans. Inst. Chem. Eng.*, **47**, T-251 (1969).
Friedel, L., "Pressure Drop during Gas/Vapor-Liquid Flow in Pipes," *Int. Chem. Eng.*, **20**, 352 (1980).
Gal-Or, B., and S. Waslo, "Hydrodynamics of an Ensemble of Drops (or Bubbles) in the Presence or Absence of Surfactants," *Chem. Eng. Sci.*, **23**, 1431 (1968).
Glasgow, L. A., L. E. Erickson, C. H. Lee, and S. A. Patel, "Wall Pressure Fluctuations and Bubble Size Distributions at Several Positions in an Airlift Fermentor," *Chem. Eng. Commun.*, **29**, 311 (1984).
Goodman, C. H., and H. H. Sogin, "Calibration of a Hot-Film Anemometer in Water over the Velocity Range 0.5 to 200 cm/s," *ASME Symp. on Flow—Its Measurement and Control in Science and Industry*, Pittsburgh, PA (May, 1971).
Griffith, R. M., "Mass Transfer from Drops and Bubbles," *Chem. Eng. Sci.*, **12**, 198 (1960).
Hasimoto, H., "On the Periodic Fundamental Solutions of the Stokes Equations and Their Application to Viscous Flow Past a Cubic Array of Spheres," *J. Fluid Mech.*, **5**, 317 (1959).
Herringe, R. A., and M. R. Davis, "Flow Structure and Distribution Effects in Gas-Liquid Mixture Flows," *Int. J. Multiphase Flow*, **4**, 461 (1978).
Hsu, Y. C., and M. P. Dudukovic, "Gas Holdup and Liquid Recirculation in Gas-Lift Reactors," *Chem. Eng. Sci.*, **35**, 135 (1980).
Hughmark, G. A., "Pressure Drop in Horizontal and Vertical Cocurrent Gas-Liquid Flow," *I. & E. C. Fundam.*, **2**, 315 (1963).
Ishii, M., and N. Zuber, "Drag Coefficient and Relative Velocity in Bubbly, Droplet or Particulate Flows," *AIChE J.*, **25**, 843 (1979).
Jones, A. G., "Liquid Circulation in a Draft-Tube Bubble Column," *Chem. Eng. Sci.*, **40**, 449 (1985).
Jones, G. T., L. A. Glasgow, and L. E. Erickson, "Local Liquid Velocity Measurements in a Split Cylinder Airlift Column," ACS Conf. paper, New Orleans (Sept., 1987).
Jones, O. C., and J.-M. Delhaye, "Transient and Statistical Measurement Techniques for Two-Phase Flows," *Int. J. Multiphase Flow*, **3**, 89 (1976).
Kawase, Y., B. Halard, and M. Moo-Young, "Theoretical Prediction of Volumetric Mass Transfer Coefficients in Bubble Columns for Newtonian and Non-Newtonian Fluids," *Chem. Eng. Sci.*, **42**, 1609 (1987).
Kleinstreuer, C., and T. Poweigha, "Modeling and Simulation of Bioreactor Process Dynamics," *Adv. in Biochem. Eng. Biotech.*, **30**, 91 (1984).
Koide, K., S. Hiroyuki, and S. Iwanoto, "Gas Holdup and Volumetric Liquid-Phase Mass Transfer Coefficient in Bubble Column with Draught Tube and with Gas Dispersion into Annulus," *J. Chem. Eng. Japan*, **16**, 407 (1983a).
Koide, K., K. Kuremastsu, L. Iwamoto, Y. Iwata, and K. Horibe, "Gas Holdup and Volumetric Liquid-Phase Mass Transfer Coefficient in Bubble Column with Draught Tube and with Gas Dispersion into Tube," *J. Chem. Eng. Japan*, **16**, 413 (1983b).
Koide, K., S. Iwamoto, Y. Takasaka, S. Matsuura, I. Takahasi, M. Kimura, and H. Kubota, "Liquid Circulation, Gas Holdup and Pressure Drop in Bubble Column with Draught Tube," *J. Chem. Eng. Japan*, **17**, 611 (1984).
Koide, K., M. Kimura, H. Nitta, and H. Kawabata, "Liquid Circulation in Bubble Column with Draught Tube," *J. Chem. Eng. Japan*, **21**, 393 (1988).
Lee, C. H., L. A. Glasgow, L. E. Erickson, and S. A. Patel, "Liquid Circulation in Airlift Fermentors," *Biotechnology Processes, Scale-Up and Mixing, AIChE Symp. Ser.*, **50** (1987).
Lockhart, R. W., and R. C. Martinelli, "Proposed Correlation of Data for Isothermal Two Phase, Two-Component Flow in Pipes," *Chem. Eng. Prog.*, **45**, 39 (1949).
Lombardi, C., and E. Pedrocchi, "A Pressure Drop Correlation in Two-Phase Flow," *Energia Nucleare*, **19**, 91 (1972).
Love, D. L., "Improved Two-Phase Flow Calculations," *Oil and Gas J.*, 79 (Jan. 7, 1974).
Lundgren, T. S., E. M. Sparrow, and J. B. Starr, 'Pressure Drop Due to the Entrance Region in Ducts of Arbitrary Cross Section," *Trans. ASME, J. Basic Eng.*, **86**, 620 (1964).
Malfait, J., D. Wilcox, D. Mercer, and L. Barker, "Cultivation of a Filamentous Mold in a Glass Pilot-Scale Airlift Fermentor," *Biotech. Bioeng.*, **23**, 863 (1981).
Merchuk, J. C., and Y. Stein, "Local Hold-Up and Liquid Velocity in Air-Lift Reactors," *AIChE J.*, **27**, 377 (1981).
Merchuk, J. C., and Y. Stein, "Local Hold-Up and Liquid Velocity in Air-Lift Fermentor," *Biotech. Bioeng.*, **22**, 1189 (1981).
Moujaes, S., and R. S. Dougall, "Experimental Investigation of Cocurrent Two-Phase Flow in a Vertical Rectangular Channel," *Can. J. Chem. Eng.*, **65**, 705 (1987).
Onken, U., and P. Weiland, "Airlift Fermenters: Construction, Behavior and Uses," *Developments in Biotech Processes*, Vol. 1, A. Misrahi and A. van Wezel, eds., Alan R. Liss, 67 (1983).
Orazem, M. E., L. T. Fan, and L. E. Erickson, "Bubble Flow in the Downflow Section of an Airlift Tower," *Biotech. Bioeng.*, **21**, 1579 (1979).
Pal, S. S., A. K. Mitra, and A. N. Roy, "Pressure Drop and Holdup in Vertical Two-Phase Cocurrent Flow with Improved Gas-Liquid Mixing," *Ind. Eng. Chem. Process Des. Dev.*, **19**, 67 (1980).
Popovic, M., and C. W. Robinson, "The Specific Interfacial Area in External-Circulation Loop Airlift and a Bubble Column: II. Carboxymethyl Cellulose/Sulphite Solution," *Chem. Eng. Sci.*, **42**, 2825 (1987).
Ranz, W. E., "Friction and Transfer Coefficients for Single Particles and Packed Beds," *Chem. Eng. Prog.*, **48**, 247 (1952).
Schrock, V. E., "Radiation Attenuation Technique in Two-Phase Flow Measurements," *Two-Phase Flow Instrumentation*, ASME/AIChE Heat Transfer Conf., Minneapolis, **24** (1969).
Serizawa, A., I. Kataoka, and I. Michiyoshi, "Turbulence Structure of Air-Water Bubbly Flow: I. Measurement Techniques," *Int. J. Multiphase Flow*, **2**, 221 (1975).
Sherwood, T. K., R. L. Pigford, and C. R. Wilke, *Mass Transfer*, McGraw-Hill, New York (1975).
Siegel, M. H., J. C. Merchuk, and K. Schugerl, "Air-Lift Reactor Analysis: Interrelationships between Riser, Downcomer, and Gas-Liquid Separator Behavior, Including Gas Recirculation Effects," *AIChE J.*, **32**, *1585 (1986)*.
Singh, R. P., K. K. Nigam, and P. Mishra, "Developing and Fully Developed Turbulent Flow Through Annuli," *J. Chem. Eng. Japan*, **13**, 349 (1980).
Slattery, J. C., *Momentum, Energy, and Mass Transfer in Continua*, R. E. Krieger Publishing Co., New York (1981).
Sukan, S. S., and G. Vardar-Sukan, "Mixing Performance of Air-Lift Fermenters against Working Volume and Draft Tube Dimensions," *Bioprocess Eng.*, **2**, 33 (1987).
Townsley, P., F. Webster, F. Kutney, P. Salisbury, G. Hewitt, N. Kawamura, L. Choi, T. Keruihara and G. Jacoli, "The Recycling Air Lift Transfer Fermenter for Plant Cells," *Biotech. Letters*, **5**, 13 (1983).
Verlaan, P., J. Tramper, and K. Van'T Reit, "A Hydrodynamic Model for an Airlift-Loop Bioreactor with External Loop," *Chem. Eng. J.*, **33**, B43 (1986).
Wallis, G. B., *One-Dimensional Two-Phase Flow*, McGraw-Hill, New York (1969).
Weiland, P., "Influence of Draft Tube Diameter on Operational Behavior of Airlift Loop Reactors," *German Chem. Eng.*, **7**, 374 (1984).
Whitaker, S., *Introduction to Fluid Mechanics*, R. E. Krieger Publishing Co., New York (1981).
Wyman, D. R., and A. A. Harms, "Statistical Uncertainty in the Radiation Diagnosis of Two-Phase Flows," *Nucl. Eng. Design*, **85**, 261 (1985).
Young, M. A., "Airlift Bioreactors: Experimental and Theoretical Analysis of Two-Phase Hydrodynamics," PhD Thesis, North Carolina State Univ. (1989).
Zick, A. A., and G. M. Homsy, "Stokes Flow Through Periodic Arrays of Spheres," *J. Fluid Mech.*, **115**, 13 (1981).
Zuber, N., and J. A. Findlay, "Average Volumetric Concentration in Two-Phase Flow Systems," *J. Heat Trans.*, **87**, 453 (1965).

Manuscript received May 14, 1990, and revision received Jan. 7, 1991.